Accepted by *ApJ*

# Collisional Stellar Dynamics Around Massive Black Holes in Active Galactic Nuclei

*Kevin P. Rauch*[1]
California Institute of Technology,
Canadian Institute for Theoretical Astrophysics, and
University of Maryland

## ABSTRACT

The dynamical evolution of nuclear star clusters containing a massive black hole is examined in the region in which physical collisions dominate other processes and the black hole dominates the potential. The numerical method features a discrete cluster of stars, fully relativistic calculation of the orbital trajectories (including an algorithm that searches for individual collisions between pairs of orbits), and the use of a series of smooth particle hydrodynamics simulations of high-velocity stellar impacts (computed independent of this work) to determine collision outcomes. In contrast to a Fokker-Planck analysis, this approach allows small-number statistics, relativistic effects, and collision dynamics to be accounted for directly and accurately. The versatility of the simulation techniques makes them usable in a range of problems; useful by-products of the routines include a simple, exact procedure for computing the integrals of motion of Kerr geodesics given their Keplerian orbital elements, and a generalized form of Kepler's Equation that is (asymptotically) valid in the Kerr geometry. We find that many grazing collisions produce very little mass loss—even when a head-on collision would lead to complete disruption—thereby creating an extended distribution of low-mass remnants. Collisional refilling of the loss cone is seen and generally dominates relaxation-induced disruptions in these systems. It is found that collisions preferentially produce a constant density core in the collisionally-dominated region of the cusp, as opposed to the $\rho \propto r^{-1/2}$ profile found in Fokker-Planck studies; the discrepancy can be traced to the simplifying assumptions typically employed by the latter approach.

*Subject headings:* black hole physics — celestial mechanics, stellar dynamics — galaxies: active — galaxies: nuclei

[1]Current Address: Dept. of Astronomy, Univ. of Maryland, College Park, MD 20742-2421.

## 1. Introduction

Recent observations (e.g., Kormendy et al. 1996; Ferrarese, Ford, & Jaffe 1996; van der Marel et al. 1997) are providing convincing evidence that many galactic nuclei contain massive dark objects (presumably massive black holes—hereafter MBHs), a hypothesis originally advanced over a quarter century ago (Lynden-Bell 1969; cf. Hoyle et al. 1964). Hubble Space Telescope observations of M87, for instance, give strong evidence of a central mass of $\sim 3 \times 10^9 M_\odot$ (Harms et al. 1994), and observations of M31 (Richstone, Bower, & Dressler 1990; Bacon et al. 1994) and the Galactic Center (Haller et al. 1996; Eckart & Genzel 1997) are consistent with central MBHs of $\sim 3 \times 10^7 M_\odot$ and $\sim 2 \times 10^6 M_\odot$, respectively. There are also strong theoretical arguments in favor of this postulate. The standard model of energy production in active galactic nuclei (AGNs), for example, invokes accretion of gas onto MBHs in the range $\sim 10^6 - 10^9 M_\odot$ as the ultimate power source in these objects, and essentially all plausible alternatives, such as supermassive stars or dense starbursts, are virtually guaranteed to produce an MBH during the course of their evolution if one is not already there (e.g., Rees 1984). Besides the observational evidence for MBHs in galactic nuclei (see Kormendy & Richstone 1995 for a review), numerical simulations of the dynamical evolution of dense nuclear star clusters—which are seen in numerous galaxies (Faber et al. 1997; Genzel et al. 1994; Lauer 1989)—indicate that they are probably unstable to the formation of moderate mass ($\sim 10^3 M_\odot$) black holes, which would subsequently grow to $\sim 10^6 - 10^8 M_\odot$ through continued consumption of stars from the surrounding cluster (Quinlan & Shapiro 1990). However, there is as yet no definitive evidence that the detected massive dark objects are in fact MBHs; proof of this will hinge on observations whose explanation requires reference to the relativistic properties of MBHs. Continued investigation of the dynamical effects of MBHs in (active) galactic nuclei and their possible observational consequences is thus well motivated.

The existence of dense star clusters in galactic nuclei makes it a near certainty that collisions between stars will play an important role in the cluster's dynamical evolution, at least at small radii, since both two-body relaxation (which leads to eventual gravothermal collapse of the core) and central MBHs will tend to drive the inner regions towards higher densities and velocity dispersions until collisional processes become significant. Historically, before accretion onto a black hole came into favor as a way to power AGNs, several authors examined the evolution of nuclear clusters (without black holes) in which, after a period of relaxation, stellar collisions became the dominant dynamical process; this was studied in part to determine if the energy released in the collisions themselves could explain the luminosity of quasars (Spitzer & Saslaw 1966; Spitzer & Stone 1967; Colgate 1967; Sanders 1970). Spitzer & Saslaw (1966) and Spitzer & Stone (1967) studied clusters with high velocity dispersions ($v_{\rm rms} \gtrsim 10^3$ km s$^{-1}$) in which collisions were presumed to be disruptive, using a simple geometric model of mass loss from stellar collisions to compute the mass liberation rate; they found a peak luminosity of $\sim 10^{45}$ erg s$^{-1}$ for a cluster of $10^8$ stars with an initial radius of 0.05 pc. Colgate (1967) pointed out that when collisions first become important, they would occur at low enough relative velocity that coalescence would occur instead of disruption, and argued that the resulting buildup of massive stars, which would subsequently lead to a high rate of supernovae, could generate enough luminosity to explain energetic AGNs; a similar study by Sanders (1970), however, reached the opposite conclusion. A common feature of these studies is that they all used simple, qualitative prescriptions to calculate the outcome of a collision. The conflicting results of Colgate and Sanders—most likely resulting from the different prescriptions each used—highlight the uncertainty that such simplifications can introduce.

Growing computer power is allowing increasingly realistic simulations of both the dynamical evolution of galactic nuclei and of the hydrodynamics of stellar collisions to be performed. Most studies of the evolution of galactic nuclei (Duncan & Shapiro 1983; David, Durisen, & Cohn 1987a,b; David & Durisen 1989; Quinlan & Shapiro 1990; Murphy, Cohn, & Durisen 1991) have used Fokker-Planck methods incorporating progressively larger numbers of dynamical processes to examine cluster evolution, taking into account such things as two-body relaxation, tidal disruption, stellar evolution and mass loss, binary formation and heating, and stellar collisions. Although these studies represent major advances over previous research, they do have limitations. We note for one that these studies assume that the cluster can at all times be described by an isotropic distribution function, $f(\mathcal{E})$; additionally, since by nature the Fokker-Planck approach is a statistical one, the above processes can only be included in an average sense. These studies have used the same or similar prescriptions for determining the outcomes of stellar collisions as used in the early studies, leaving them subject to the same uncertainties; advances in hydrodynamics simulations, however—in particular the development and application of smooth particle hydrodynamics (SPH) to the problem of stellar collisions (Benz & Hills 1987; Davies, Benz, & Hills 1991, 1992; Lai, Rasio, & Shapiro 1993)—promise to greatly alleviate this shortcoming.

The purpose of this paper is to examine the dynamical evolution of the core of a dense star cluster around a massive black hole in the region that stellar collisions dominate the evolution and the black hole dominates the potential, using a different (and more versatile) approach than has been used previously. Specifically, the cluster is modeled using a discrete collection of stars whose orbits are accurately traced using the geodesic equations of the Kerr (rotating black hole) metric. The intention is not only to compute the evolution of cluster properties such as the density profile, orbital distributions, and collisional mass release rate, but also to determine the importance of relativistic effects on the evolution. In the evolution of twisted accretion disks (Bardeen & Petterson 1975; Kumar & Pringle 1985; Pringle 1992), for instance, the Lense-Thirring precession produced by Kerr black holes causes the inner portions of the disk to align with the equatorial plane of the hole (the Bardeen-Petterson effect). Since relativistic corrections to the stellar orbits can be significant in the region under consideration, it is conceivable that the inherent anisotropy of the Kerr spacetime could manifest itself in the present case as well. Additional background discussion of Kerr effects is given in § 2.2. The use of discrete stars also makes it easy to include a stellar mass spectrum and to follow its evolution, which could be substantial (Lee & Nelson 1988). To treat the collision dynamics as accurately as possible, individual collision outcomes (characterized by the mass loss and vector change in velocity suffered by each star) were computed using fitting formulae derived from detailed SPH simulations of high velocity stellar collisions performed independently of this work by Melvyn Davies (1994). Since the use of individual stars ($\sim 3 \times 10^4$ in these simulations) does restrict the total simulation volume around the MBH, the approach adopted here can be considered complementary to Fokker-Planck analyses, which are appropriate in the opposite limit of large volumes and numbers of particles (where relativistic effects are very weak and phase space is well populated).

As explained in § 3, collisions between stars are found using a hybrid method in which collisions between the innermost ($\sim$ 500) cluster stars are solved for directly, without approximation, with collisions between the remaining stars being randomly forced to occur at a dynamically computed rate that takes account of the current cluster density profile. This approach offers several advantages. First is its ability to allow the stars closest to the black hole, which are affected most strongly by relativistic effects, to be treated with a minimum of approximations, which could mask or bias subtle relativistic influences. Second, since finding collision events explicitly (especially between general quasi-elliptical Kerr geodesics, as is being done here) is expensive, the use of a zone of randomly generated collisions allows a much larger total volume and number of stars to be followed. It is also versatile in that each individual strategy has enough flexibility to be used in several different ways; the simulations presented here represent one specific application. The collision finding algorithm, for instance, can be used to evolve a cluster undergoing relativistic two-body relaxation (gravitational 'collisions') in the vicinity of a Kerr black hole. Another application would be to sticky-particle type simulations in a Kerr environment, which could be useful for investigating the evolution of relativistic disks, for example. The adaptive behavior of the routine which randomly selects collisions makes it usable even when the distribution is changing rapidly or is significantly anisotropic. Also generically useful are the modified Kepler's Equation incorporating relativistic corrections and the simple procedure for computing the geodesic constants of motion from the Keplerian orbital elements, both of which are used by the collision finding routine.

The remainder of this paper is organized as follows. In § 2, the basic dynamical processes relevant to the simulations are briefly reviewed; some discussion of the properties of Kerr black holes is also given. Section 3 explains in detail how the simulations were performed. Results and discussion are given in § 4, and conclusions are offered in § 5. Finally, Appendix A derives the modified Kepler's Equation, and Appendix B presents the SPH fitting formulae used and a discussion of related issues.

Except where units are specifically given, this paper uses dimensionless variables defined by taking $G = c = M = 1$, where $M$ is the mass of the black hole; hence distances are measured in units of $GM/c^2$, time in units of $GM/c^3$, and velocities in units of $c$.

## 2. Stellar Dynamical Processes in AGNs

### 2.1. Dynamical Influences on Cluster Evolution

The physical processes which in principle can affect the evolution of a star cluster include two-body relaxation, tidal (i.e., loss cone) effects (if the cluster contains a black hole), stellar collisions and mergers, stellar evolution and mass loss (supernovae), star formation, the creation of binaries and heating through binary encounters, and in the case of a cluster in an AGN, possibly also interactions with an accretion disk. For highly relativistic clusters energy losses due to gravitational radiation can also be important (Quinlan & Shapiro 1989; Lee 1993), although this is mainly relevant for clusters composed of compact objects such as neutron stars or stellar mass black holes, not main sequence stars. In the cluster cores treated in these simulations, which extend to distances of $r_{\rm SC} \sim 10^3 - 10^5$ from the MBH depending on the model, the typical velocity dispersion is quite high, $v_{\rm rms} \sim v_{\rm orb} \gtrsim r_{\rm SC}^{-1/2} \sim 0.01 \equiv 3,000$ km s$^{-1}$ (the choice of notation $r_{\rm SC}$ will become clear in § 3); this is much larger than the surface escape speed of solar type stars, $v_{\rm esc} \sim 600$ km s$^{-1}$. Because of this, binaries and relaxation effects will be unimportant compared to collisions in determining the local dynamical equilibrium, and collisions will lead to eventual disruption of stars instead of mergers. As explained in § 3.5, in some simulations relaxation is included in a limited way to account for injection of new stars into the inner core from the exterior regions of the cluster, but it is otherwise neglected. The short evolution times of most of these cores ($\sim 10^6 - 10^8$ yr) should make stellar evolution processes of little importance—especially since the more massive, quickly evolving stars also tend to be the first to collide due to their larger geometric cross-sections—and it was not included here (see also § 4); star formation is similarly neglected.

If the AGN contains an accretion disk, it will affect the evolution of the cluster through star-disk interactions (SDIs; Syer et al. 1991; Karas & Vokrouhlický 1993; Artymowicz, Lin,

& Wampler 1993; Rauch 1995). The main effects are circularization of the orbits and their alignment with the plane of the disk (due to the drag force suffered by the stars each disk crossing). As noted by Rauch (1995), either SDIs or physical collisions can dominate in this instance. That work considered the limit in which SDIs dominate the dynamical evolution; this paper treats the opposite limit, in which physical collisions dominate. The case in which both effects are of comparable importance will be examined in future work.

If evolution is dominated by relaxation, the effect of a central black hole (treated as a Newtonian point mass) on an isotropic cluster is to create a density cusp $\rho \propto r^{-7/4}$ within the hole's sphere of influence, $r_{\rm h} \sim v_{\rm rms}^{-2}$ (Bahcall & Wolf 1976). However, the existence of a black hole horizon—and, for MBHs $\lesssim 10^9 M_\odot$, a tidal radius—creates a loss cone which will modify (flatten) this cusp at small radii (Frank & Rees 1976; Lightman & Shapiro 1977; Cohn & Kulsrud 1978), due to tidal disruption or direct consumption of stars entering the loss cone. Collisions will further modify the cusp solution, and one of the results of these calculations will be a quantitative estimate of the cusp profile in the vicinity of the MBH. Hills (1975) suggested tidal mass loss and subsequent accretion of gas onto the black hole as a possible way to power AGNs. It is now generally agreed that this mechanism liberates insufficient amounts of gas to account for the more powerful AGNs unless collisional processes predominate. By incorporating the results of SPH simulations of colliding stars into the analysis, one aim of this paper is to realistically estimate the mass liberation rate produced by these collisions. Tidal mass loss is also accounted for in the calculations, but as shown in § 4 this mass loss rate is significantly below the amount lost in collisions.

To summarize, in all calculations presented here disruptive collisions dominate the dynamical evolution of the cluster, and relaxation enters in a very limited way. Although expected to be of minor importance, tidal effects are also included as the cost of doing so is trivial in our approach. To determine the range of cluster densities and radii over which these assertions are valid, we now compare the relative importance of these three processes more carefully. To this end, it is useful to define dimensionless, orbit-averaged collision, relaxation, and tidal depths defined by $\tau_i = \oint \mathrm{d}t(r)/t_i(r)$, where the corresponding timescale for process $i$ is $t_i$ and the integral is over a complete orbit. Thus $1/\tau_{\rm coll}$ is the average number of orbits traversed between collisions, $t_{\rm orb}/\tau_{\rm r}$ is the orbit-averaged relaxation time, and process $i$ dominates process $j$ whenever $\tau_i \gg \tau_j$. The respective timescales are given by $t_{\rm coll} \sim (n_\star \sigma v_{\rm rel})^{-1}$, $t_{\rm r} \sim v_{\rm orb}^3/[15 G^2 m_\star^2 n_\star \ln(0.4 N_\star)]$, and $t_{\rm t} \sim (1-e^2) t_{\rm r}$, where $n_\star$ is the number density of stars, $\sigma \approx 4\pi R_\star^2$ is the collision cross-section (neglecting gravitational focusing, since $v_{\rm rel} \gg v_{\rm esc}$), $v_{\rm rel}$ ($\approx \sqrt{2}\, v_{\rm orb}$ for an isotropic cluster) is the typical relative velocity between stars, $v_{\rm orb} = [2/r - 1/a]^{1/2}$ is the star's orbital speed, and $N_\star$ is the total number of stars in the cluster. The semi-major axis and eccentricity of the orbit are $a$ and $e$. The tidal timescale, $t_{\rm t}$, is the typical time needed for the orbit to diffuse into the loss cone (assuming the loss cone orbit has $e \approx 1$). Note that $\tau_{\rm t}$ for an orbit with $a(1-e) \sim r_{\rm t}$ (where $r_{\rm t} \approx 2R_\star(M/m_\star)^{1/3}$ is the tidal radius) is essentially the function '$q(E)$' of Lightman & Shapiro (1977), defined as the ratio of the mean square change in angular momentum per orbital period due to relaxation to the width of the loss cone itself; thus $1/(1+\tau_{\rm t})$ is approximately the fraction of orbits lying near the loss cone which enter it (and disrupt) each orbital period. Assuming $n_\star = 10^6 n_6 (r/1\ {\rm pc})^{-7/4}\ {\rm pc}^{-3}$ and $M = 10^8 M_8\, M_\odot$, the numerical values of these depths are approximately

$$\tau_{\rm coll} \approx 2\times 10^{-4}\, n_6 M_8^{-3/4} \left(\frac{m_\star}{M_\odot}\right)^{4/3} (3-e)\, r_{\rm min}^{-3/4}, \tag{1}$$

$$\tau_{\rm r} \approx 2\times 10^{-14}\, n_6 M_8^{-3/4} \left(\frac{m_\star}{M_\odot}\right)^{2} \left(1+\frac{e}{3}\right)^{2} a^{5/4}, \tag{2}$$

$$\tau_{\rm t} \approx 5\times 10^{-15}\, n_6 M_8^{-3/4} \left(\frac{m_\star}{M_\odot}\right)^{2} (1-e)^{-1}\, a^{5/4}, \tag{3}$$

where $r_{\rm min} = a(1-e)$. Note that $a$ is still in units of $M$; in physical units, $M = 5\times 10^{-6} M_8$ pc. The condition $\tau_{\rm coll} \gtrsim \tau_{\rm r}$ implies $a \lesssim 10^5 (1-e)^{-3/8}$ (assuming solar type stars)—only weakly dependent on $e$; it follows that collisions are more important than relaxation in determining the distribution function at radii $r \lesssim 2\times 10^5 = 1 M_8$ pc, independent of the absolute density. Similarly, tidal effects are more important than relaxation for $r \lesssim r_{\rm crit}$, where $\tau_{\rm t} \sim 1$ for $r_{\rm crit}(1-e) \sim r_{\rm t}$, which implies $r_{\rm crit} \sim 4\times 10^6\, n_6^{-4/9} M_8^{1/12}$ (again assuming solar type stars). To complete the triad, $\tau_{\rm coll} > \tau_{\rm t}$ implies $a \lesssim 3\times 10^5\,(1-e)^{1/8}$. Hence in the region where collisions dominate over relaxation, they also dominate loss cone effects, except for rare, very high eccentricity orbits that violate the last inequality. Motivated by these considerations, the cluster initial conditions were chosen to be a truncated $r^{-7/4}$ power law with $a_{\rm min} \sim r_{\rm t}$ and $a_{\rm max} \sim 3\times 10^5$ (see § 3.1).

The numerical values for the orbit-averaged timescales, $t_i = t_{\rm orb}/\tau_i$, are

$$t_{\rm coll} \approx 0.5\, n_6^{-1} M_8^{7/4} \left(\frac{m_\star}{M_\odot}\right)^{-4/3} (3-e)^{-1}(1-e)^{-3/2} r_{\rm min}^{9/4}\ {\rm yr}, \tag{4}$$

$$t_{\rm r} \approx 5\times 10^{9}\, n_6^{-1} M_8^{7/4} \left(\frac{m_\star}{M_\odot}\right)^{-2} \left(1+\frac{e}{3}\right)^{-2} a^{1/4}\ {\rm yr}, \tag{5}$$

$$t_{\rm t} \approx 2\times 10^{10}\, n_6^{-1} M_8^{7/4} \left(\frac{m_\star}{M_\odot}\right)^{-2} (1-e) a^{1/4}\ {\rm yr}. \tag{6}$$

These specific relations are only valid within the $(r^{-7/4})$ cusp, which extends to a radius $r_{\rm h} \sim 1\times 10^6 n_6^{-4/5} M_8^{-1/5} \approx 5\, n_6^{-4/5} M_8^{4/5}$ pc, outside of which the cluster, not the black hole, dominates the potential. (A cluster of equal mass stars is also assumed; also note that gravitational focusing has been neglected in eq. [4].) Table 1 lists $r_{\rm h}$ and the maximum radii for which each timescale is shorter than a Hubble time, $\sim 10^{10}$ yr, for several hole masses, assuming solar stars and $e^2 = 0.5$ (the mean value for an isotropic cluster). Astrophysically the mass $M = 10^6 M_\odot$ could correspond to a modest Seyfert galaxy or to the Galactic Center, $M = 3\times10^7 M_\odot$ to a bright Seyfert or M31, and $M = 10^9 M_\odot$ to a typical quasar or a nucleus such as M87's. Note that collisions are always important in the cusp and that relaxation processes are negligible for nuclei with very massive black holes. Since the $r^{-7/4}$ cusp is created on a relaxation timescale, the last point suggests that a well-formed cusp has not had time to develop in these nuclei; however, initial adiabatic growth of the black hole, which occurs on timescales much shorter than $t_{\rm r}$, creates a similar cusp, between $r^{-3/2}$ for isotropic orbits to $r^{-9/4}$ for purely circular orbits (Young 1980; cf. Quinlan, Hernquist, & Sigurdsson 1995). The $r^{-7/4}$ form should therefore provide a reasonable description of the cusp even in this case.

### 2.2. Effects of Kerr Black Holes

One feature of the collision code is its use of a fully relativistic formalism for the computation of stellar orbital trajectories and collision center-of-mass frames, using the Kerr metric to model the spacetime environment. This is the appropriate model for astrophysical black holes where they dominate the gravitational potential, as in these simulations. This section gives a short review of the physics of Kerr black holes. For a detailed review of black holes in an AGN environment, see Blandford (1987).

In general relativity, all (time-independent) black holes are uniquely specified by three parameters (e.g., Misner, Thorne, & Wheeler 1973): their mass, $M$, angular momentum,

Table 1. Maximum Radii for Dynamical Evolution Within a Hubble Time

| | $n_6^{4/5} r_{\rm h}$ | | $n_6^{-4/9} r_{\rm coll}$ | | $n_6^{-4} r_{\rm r}$ | | $n_6^{-4} r_{\rm t}$ | |
|---|---|---|---|---|---|---|---|---|
| $M$ ($M_\odot$) | ($M$) | (pc) | ($M$) | (pc) | ($M$) | (pc) | ($M$) | (pc) |
| $1\times10^6$ | $3\times10^6$ | 0.2 | $3\times10^6$ | 0.15 | $> r_{\rm h}$ | $> r_{\rm h}$ | $> r_{\rm h}$ | $> r_{\rm h}$ |
| $3\times10^7$ | $2\times10^6$ | 2 | $2\times10^5$ | 0.3 | $4\times10^5$ | 0.5 | $5\times10^4$ | 0.06 |
| $1\times10^9$ | $1\times10^6$ | 40 | $1\times10^4$ | 0.7 | $< 1$ | $\cdots$ | $< 1$ | $\cdots$ |

$J$, and charge, $Q$, with the additional requirement that $Q^2 + (J/M)^2 \leq M^2$ (violation of this constraint results in a naked singularity, not a black hole). In astrophysical contexts, $Q$ is essentially guaranteed to be unimportant dynamically, as even a small relative excess of charge would be quickly quenched by accretion of charged particles due to the greatly mismatched strengths of gravity and electromagnetism. The angular momentum of the hole, however, can be substantial. (The remainder of this discussion will assume $Q = 0$ and define $j = J/M^2$.) This is particularly true for black holes in AGNs, which are expected to be spun up by accretion of matter (as from an accretion disk) to near maximal values, $j \sim 1$, regardless of their initial $j$ (Bardeen 1970; Thorne 1974).

Both Kerr and Schwarzschild ($j = 0$) black holes exert qualitatively new effects on orbits compared to Newtonian gravity. In the Schwarzschild case spherical symmetry ensures that orbits still lie in a plane, but due to precession bound orbits no longer close on themselves; asymptotically far from the hole this precession amounts to $6\pi/[a(1-e^2)]$ rad per orbit (cf. eq. [A21]). In the Kerr case the angular momentum introduces a preferred direction, and in general orbits no longer lie in a plane, although for distant orbits the motion can be well approximated by a slowly rotating planar orbit. Physically this non-planarity (or precession of the effective orbital plane about the spin axis of the hole) is the result of Lense-Thirring precession. As mentioned in § 1, in an AGN environment Lense-Thirring precession can have important consequences, such as the Bardeen-Petterson effect.

Another qualitatively new feature is the creation of a region of unstable orbits. In the Schwarzschild case circular orbits inside $6M$ are unstable (and do not exist at all inside $3M$), and small inward perturbations will cause them to spiral into the hole; additionally no quasi-elliptical orbits exist with $r_{\rm min} < 4M$. For Kerr holes these radii depend on both $j$ and the orbital inclination, but qualitatively speaking, retrograde orbits become unstable at larger radii and prograde orbits are stable to smaller radii. A dynamical consequence of this is the creation of a loss cone even for objects which cannot be tidally disrupted by the hole. A final new property we will mention is the presence of negative energy orbits around Kerr holes, which exist only within the ergosphere (the region near the horizon in which frame-dragging forces all test particles to rotate in the sense of the hole); the significance of these orbits is explained below.

In a dynamical sense, Schwarzschild black holes are 'dead'—their potentials can power AGNs through release of binding energy of inspiraling matter (up to $\sim 6\%$ of the rest mass), but their own rest-mass energy cannot be released. This is not the case for Kerr holes, whose spin energy can be extracted, up to a point, by several mechanisms (decreasing $M$ in the process). One of these is the Penrose process (Penrose 1969), in which a particle on a negative energy orbit can cross the horizon and reduce the hole's mass. Energy can also be extracted electromagnetically (Blandford & Znajek 1977). In the calculations presented here, however, such effects have little chance to operate, and in terms of possible influences on cluster evolution, the salient relativistic effects are precession and possibly loss cone effects; collision dynamics might also be influenced by the anisotropy of the Kerr spacetime (frame-dragging effects). Note that optical observations can only resolve distances $\sim v_{\rm obs}^{-2} \sim 1 \times 10^5 (v_{\rm obs}/10^3 \text{ km s}^{-1})^{-2} \sim 1 M_8 (v_{\rm obs}/10^3 \text{ km s}^{-1})^{-2}$ pc, on which scales these effects will be quite small; *direct* observation of them is therefore unlikely.

## 3. Numerical Method

The numerical simulations divided each cluster into four distinct radial regions. The innermost zone, to be termed the tidal region, contains few (if any) stars and is the volume around the black hole in which entering stars will be tidally disrupted. Outside this zone (which extends to a radius $r_{\rm t}$) are the innermost cluster stars, which lie in what will be called the 'deterministic collisions' (DC) region; in this zone, physical collisions between the stars were searched for iteratively using the collision algorithm described in § 3.3; the outer boundary of this zone, $r_{\rm DC}$, is dynamically adjusted during the simulation so that the total number of stars entering it remains constant. Exterior to the DC region lies the 'statistical collisions' (SC) region, in which individual collisions were not solved for iteratively but rather were forced to occur at a rate consistent with each star's orbit-averaged collision timescale; this zone extended out to some fixed radius, $r_{\rm SC}$, set by the total number of stars in the simulation. Finally, the outermost region, labeled the 'reservoir,' consisted of all cluster stars not explicitly included in the calculations. This region provided the boundary conditions used (by the steady state runs) to compute the rate at which relaxation would inject stars into the inner, simulated core; the region's own dynamical evolution, however, was not followed. A detailed description of each zone is given in the following subsections.

### 3.1. Fundamental Parameters and Initial Conditions

Each simulation is characterized by the following elements:

1. the mass $M$ and angular momentum $j$ of the black hole,
2. the initial distribution function of the cluster, $f(\mathcal{E}, L, L_z)$,
3. the initial stellar mass spectrum,
4. the number of stars in the DC (§ 3.3) and SC (§ 3.4) zones, and
5. the presence (or absence) of the outer cluster reservoir (§ 3.5).

For details on the determination of collision products, which was done the same way in all simulations, see Appendix B.

Black hole masses in the simulations ranged from $10^6$ to $10^9 M_\odot$, roughly covering the range suggested by observations of galactic nuclei (see § 1). Most simulations used $j = 1$, for which any precession-induced effects would be maximized; to judge sensitivity to the black hole's spin, a few runs were repeated using $j = 0$.

In a Newtonian point-mass potential, $\Psi = 1/r$, all five orbital elements—the semi-major axis, $a$, eccentricity, $e$, inclination, $i$, argument of periapse, $\omega$, and argument of the ascending node, $\Upsilon$—are integrals of the motion. The correspondence to energy and angular momentum is $\mathcal{E} = 1/(2a)$, $L^2 = a(1-e^2)$, and $L_z = L\cos i$. We are using the conventions that $\mathcal{E} > 0$ is the binding energy and that $0 \le i \le \pi$, where $i = 0$ corresponds to a prograde orbit in the equatorial plane of the hole and $i = \pi$ to a retrograde orbit in that plane. In the Kerr spacetime geometry, geodesics possess only three integrals, which for quasi-elliptical orbits can be equated with $a, e$, and $i$—or, (almost) equivalently, $\mathcal{E}, L$, and $L_z$—with precession effects leading to non-conservation of $\omega$ and $\Upsilon$. (Strictly speaking, $L$ is not conserved for Kerr orbits; cf. Appendix A.) The simulation code was equipped to create clusters with a distribution function (in an externally imposed Newtonian potential $\Psi = 1/r$) of the form

$$f(\mathcal{E}, L, L_z) = \begin{cases} K\mathcal{E}^{n-3/2}\,\exp[pL^2/L_{\rm max}^2(\mathcal{E})]\,\exp[qL_z/L], & \mathcal{E}_{\rm min} \le \mathcal{E} \le \mathcal{E}_{\rm max}; \\ 0, & \text{otherwise,} \end{cases} \tag{7}$$

where $L_{\rm max}^2(\mathcal{E}) = 1/(2\mathcal{E})$ is the maximum possible angular momentum for an orbit of energy $\mathcal{E}$ and the normalization,

$$K = \frac{(n-3)pqN_\star}{\sqrt{2}\,\pi^3(\exp[p]-1)\sinh q\,(\mathcal{E}_{\rm max}^{n-3} - \mathcal{E}_{\rm min}^{n-3})}, \tag{8}$$

is such that the total number of stars in the cluster is $\int f\,\mathrm{d}^3\boldsymbol{r}\,\mathrm{d}^3\boldsymbol{v} = N_\star$. As explained below, $p$ and $q$ are anisotropy parameters for velocity space and real space, respectively, and $n$ is the power law index of the radial density profile.

The value of $K$ can be easily derived as follows. Create polar coordinates in both real space, $(r, \theta, \phi)$, and velocity space, $(v, \eta, \xi)$. It is convenient to let $\cos\eta = (\boldsymbol{r}\cdot\boldsymbol{v})/(rv)$ and $\xi$ be the corresponding azimuthal angle. By transforming the coordinates $(r, \theta, \phi, v, \eta, \xi) \to (\mathcal{E}, L, L_z, v,\, \phi,\, \xi)$, noting that $\mathcal{E} = 1/r - v^2/2$, $L = rv\sin\eta$, and $L_z = rv\sin\theta\sin\eta\sin\xi$, and then integrating over $\mathrm{d}v\,\mathrm{d}\phi\,\mathrm{d}\xi$, one finds $\int \mathrm{d}^3r\,\mathrm{d}^3v \to (\sqrt{2}\,\pi)^3 \int \mathcal{E}^{-3/2}\,\mathrm{d}\mathcal{E}\,\mathrm{d}L\,\mathrm{d}L_z$ (each integral being done over the full range of each variable), from which the result for $K$ follows. Since $f(\mathcal{E}, L, L_z)/N_\star$ can also be thought of as the joint probability distribution for the orbital parameters $a, e$, and $i$, it follows that the probability distributions of $a, e$, and $i$ are independent and given by $P(a) = (3-n)a^{2-n}/[a_{\rm max}^{3-n} - a_{\rm min}^{3-n}]$ (where $2\,a_{\rm max} = 1/\mathcal{E}_{\rm min}$ and $2\,a_{\rm min} = 1/\mathcal{E}_{\rm max}$), $P(e) = 2pe\exp[-pe^2]/(1-\exp[-p])$, and $P(i) = q\sin i\,\exp[q\cos i]/(2\sinh q)$. By creating the appropriate number of orbits with elements drawn from these distributions, a cluster with the distribution function (7) will be produced. Note that although this formalism is entirely Newtonian, the orbits themselves were created using a procedure appropriate for the Kerr metric; for details, see Appendix A.

The specific analytic form of equation (7) was chosen for its simplicity, ease in producing the desired initial density profile, and for its ability to model the overall effects of a cluster evolving in the presence of an accretion disk (cf. § 2.1). For $p = q = 0$, $f = f(\mathcal{E})$ only and the cluster is isotropic in both real and velocity spaces. For $p \neq 0$ the velocity dispersion is anisotropic, with orbits becoming increasingly radial on average as $p$ tends to large negative values and increasingly circular for large positive values of $p$; in real space the cluster remains spherically symmetric. For $q \neq 0$ symmetry in real space is broken, with orbits being preferentially retrograde for $q < 0$ and prograde for $q > 0$. To good approximation, the density $\rho(r,\theta) = \int f\,{\rm d}^3\boldsymbol{v}$ scales as $\rho \propto r^{-n}$ for $a_{\rm min} \le r \le a_{\rm max}$ (and fixed $\theta$), independent of $p$ and $q$. In fact, all simulations reported here used $q = 0$ for the initial cluster; the value of $p$ ranged from 0 to 10. Previous theoretical investigations into the equilibrium distribution function of a star cluster around a black hole, each making slightly different assumptions, give values of $n$ in the range $n \sim 3/2 - 5/2$ (Peebles 1972; Bahcall & Wolf 1976; Young 1980; Quinlan et al. 1995). All runs presented here used $n = 7/4$, the Bahcall-Wolf result, with $N_\star$ chosen so that $\rho(1\,{\rm pc}) \approx 10^4 - 10^6\ M_\odot\ {\rm pc}^{-3}$, in line with observations of nuclear star clusters (Lauer et al. 1995). The values $a_{\rm min} \sim 2r_{\rm t}$ and $10^5 \lesssim a_{\rm max} \lesssim 10^6$ were used (cf. § 2.1).

Most simulations used (initially) equal solar mass stars. When a range of initial masses was included, a Salpeter mass function with $0.4M_\odot \le M \le 4M_\odot$ was used for convenience, and the orbital distributions were assumed to be mass-independent.

### 3.2. The Tidal Zone

The tidal zone, which is normally devoid of stars, extends from the event horizon of the black hole out to the tidal radius of the cluster stars, and is the region within which a passing star will be tidally disrupted by the hole. Since the tidal radius $r_{\rm t} \approx 2R_\star(M/m_\star)^{1/3} = 4.4M_8^{-2/3}(m_\star/M_\odot)^{1/3}$ (assuming $R_\star \propto m_\star^{2/3}$) is mass-dependent, this region is of definite size only for clusters with equal mass stars. During the simulations, $r_{\rm t}$ was computed individually for each star, and whenever a collision placed a surviving star on an orbit passing within its own $r_{\rm t}$, it was removed from the simulation and its mass added to the 'tidally disrupted' mass total, $M_{\rm t}$. Studies of the dynamics of tidal disruptions (e.g., Evans & Kochanek 1989; Laguna et al. 1993) show that very nearly half of the mass $M_{\rm t}$ will eventually be accreted by the black hole, the remainder being ejected from its vicinity. When setting up the cluster initially, randomly drawn orbits crossing $r_{\rm t}$ were simply rejected and redrawn; setting $a_{\rm min} > r_{\rm t}$ helps to prevent this from happening in the first place. When adding stars from the reservoir (see § 3.5) *during* a simulation, however, such orbits were not rejected; instead, the associated mass was immediately added to $M_{\rm t}$, and no star was added to the inner core at that time. This procedure allows the mass loss rate due to stars entering the tidal loss cone, $\dot{M}_{\rm t}$, to be realistically estimated (i.e., within a factor of a few) and compared to the collisional mass liberation rate, $\dot{M}_{\rm coll}$. In the steady state simulations, the ratio of the two mass loss rates (assuming an isotropic cluster with a constant density core, the latter being implied by the results of these simulations themselves) should be roughly $\dot{M}_{\rm t}/\dot{M}_{\rm coll} \sim L_{\rm t}^2/L_{\rm SC}^2$—i.e., the fraction of orbits inside $r_{\rm SC}$ which also cross $r_{\rm t}$—the $L_i$ being defined such that orbits with $L < L_i$ pass inside $r_i$. Overall the tidal zone was expected to play a small role in the simulations, and this was indeed found to be the case. In most simulations, the tidal radius was small and close to the horizon, and in all cases it turned out that $\dot{M}_{\rm t} \ll \dot{M}_{\rm coll}$ (see § 4).

### 3.3. The 'Deterministic Collisions' Zone

The DC zone is not so much a specific region of space as it is a region of orbital parameters. It consists merely of those $N_{\rm DC}$ stars with the smallest periapses, and extends from the inner boundary of the cluster (set by the tidal radius) out to a radius $r_{\rm DC}$ determined by $N_{\rm DC}$ and by the current conditions within the cluster. In this region actual collisions between the stars are solved for, without approximation. This is done by advancing each star in the DC region along its quasi-periodic geodesic trajectory (also computed exactly from the equations of motion in the Kerr geometry, using the method described in Rauch & Blandford [1994]) and searching for close encounters between all overlapping pairs of orbits; the precise method used to accomplish this is given in complete detail below. Ideally (given unlimited computing power!) one would set $N_{\rm DC} = N_\star$ and solve for the true collisions over the entire cluster; in practice the algorithm used to sift through the orbits in search of collisions was limited to $N_{\rm DC} \sim 500$, for which runs covering physically worthwhile periods of time took $\sim 1$ week on a state-of-the-art workstation. Although not large by N-body standards, this number did allow a significant portion of the innermost region of the cluster—the part which can be affected by relativistic effects and small-number statistics most strongly—to be treated virtually without approximation, aside from the uncertainties in the SPH fitting formulae. It should also be remembered that unlike Newtonian N-body simulations, in the present case the gravitational force is not $1/r^2$, coordinate time is not the computationally convenient independent variable, and in general the orbits being followed neither lie in planes nor close on themselves, all of which make the problem of searching for collisions considerably more challenging (and time-consuming). Since it was nonetheless necessary to extend the radial range and total number of stars present in the simulations, an intermediate region that could contain $\gtrsim 10^4$ stars was created in which collisions were not solved for but were forced to occur at a self-consistent rate; the treatment of this region is described in § 3.4.

In broad terms the functioning of the collision finder can be understood as follows. Imagine separating the continuous geodesic trajectory of each star into a series of segments, each beginning at one periapse and extending to the next (future) one; for orbits lying far from the black hole these segments are nearly ellipses and have a well-defined orbital plane, but in general neither of these properties hold. Now consider finding all collisions (or close encounters) between a specific pair of stars in the DC zone. Obviously, only pairs of stars whose orbits overlap radially need be considered, for they cannot possibly collide otherwise; likewise, only segment pairs which overlap in time need be examined. Thus by considering in turn each successive orbital segment of one star and finding those segments of another star's orbit which overlap it in time, an exhaustive search for collisions between that pair of stars can be made; this is the basic strategy used by the collision finding routine. What remains to be worked out is an efficient method for finding close encounters between any given pair of orbital segments—or more appropriately, since in fractional terms exceedingly few segments will actually have a collision point, for *rejecting* non-colliding orbital segments as quickly as possible. Although this strategy may seem rather awkward and roundabout, it manages to substantially avoid the computational problems suffered by conceptually simpler time-based algorithms. In time-based approaches, such as the step-by-step N-body integration of the evolution of a globular cluster, time is the natural variable of integration, and searching for collisions is in principle a near triviality, since at each time step the position and velocity of each particle are already known and close encounters (or nearest neighbors) can be hunted for directly. In the Kerr spacetime, however, a much more efficient solution to the geodesic equations can be obtained if radius (or, in principle, the polar angle) is used as the independent variable instead of time; when this is done the equations of motion can be recast as definite integrals, some of which can be solved (and even inverted) analytically (for details, see Rauch & Blandford 1994). Once this is done, one can efficiently find the value of coordinate time given the radius, and it is not even necessary to integrate around each orbit to find the successive times of periapse passage. In other words, since the geodesic solutions are space-based, whole series of orbits can be 'skipped' essentially for free, a property not shared by methods attempting solution by straightforward integration of the differential equations describing the geodesic. The collision finding strategy was designed to exploit the aforementioned properties of the space-based Kerr geodesic routines, making it well-suited to the problem at hand.

Synchronization presents a special problem. Since the cluster stars possess a wide range of orbital periods, keeping the orbital segments of one star in step with those of every other star requires careful treatment. This was dealt with by dynamically creating a stack frame containing, for each star, all segments of that star's orbit traversed between fixed starting and stopping times. To evolve the cluster, all collisions occurring within the given time interval were found, the starting and stopping times were incremented, and the entire process then repeated.

Clearly, quite a large number of pairs of orbital segments, $\sim (t_{\rm max}/\bar{t}_{\rm orb})N_{\rm DC}^2$ ($\sim 10^{10}$ in the simulations), where $t_{\rm max}$ is the maximum time reached in the simulations and $\bar{t}_{\rm orb}$ is an average star's orbital period, need to be examined in the course of a run; hence it is crucial to be able to discard pairs not having a collision point as quickly as possible. The heart of the collision finding algorithm lies in its application of a series of increasingly refined (and time-consuming) 'cuts' to the particular pair of segments, designed to reject as quickly as possible pairs which don't collide, without falsely rejecting pairs that do; as these are competing goals, a suitable balance between speed and accuracy needs to be achieved, and in practice acceptability was defined as a false rejection rate (the fraction of collisions not found by the algorithm) of $\lesssim 1\%$. Central to this endeavor was the development of a modified version of Kepler's Equation valid in the Kerr geometry, derived as an expansion in $\delta = 1/[a(1-e^2)]$ and valid to $O(\delta^{5/2})$. Although Kerr orbits do not, in general, lie in a plane, the non-planarity of any single orbital segment will be small as long as the orbit does not pass too close to the hole. Thus by approximating single segments as lying in a mean orbital plane defined by the star's position and velocity vectors at apoapse (where relativistic effects for a given orbit are smallest) and applying the modified Kepler's Equation, the approximate position of the star as a function of time can be economically computed. In this way the basic strategy one would use to seek a collision between two Newtonian elliptical orbits can be applied to the Kerr segments with (conceptually) only minor amendments. The modified Kepler's Equation and related formulae are derived in Appendix A.

In final detail the segment rejection algorithm works as follows. Having excluded all pairs of stars whose orbits do not radially overlap, the following cuts were applied to each pair of segments until the possibility of collision was either excluded or, in the end, confirmed. First, the modified Kepler's Equation was used to find the time intervals during which each star resided in the radial overlap zone, in which of course all collisions must occur; if the time intervals did not overlap, the pair was rejected immediately. If this failed, use was made of the fact that each segment lies nearly in a plane. Were each orbit strictly planar, clearly they could collide only along the line of intersection of the two planes; for small deviations from planar motion, a collision point must lie somewhere *near* the line of intersection, unless the orbits are almost coplanar. Quantitative estimates of the maximum perpendicular deviation from the mean plane over a single orbit were made and used to reject segment pairs whose spatial separations at the line of intersection exceeded this limit; if a collision appeared spatially possible, the times at which the stars crossed the line of intersection were computed and exclusion was attempted on that basis. A complication over the Newtonian case is that due to general precession inside the mean orbital plane, one periapse-to-periapse orbit can cross the line of intersection more than twice (and possibly many times), each at a different radius, so that one must be careful to test all possible intersection points for overlap before rejecting a pair of orbits. Finally, if a close encounter was found by this procedure and the pair still could not be rejected, the full Kerr routines were used to find the exact point of closest approach of the orbits, using the approximate location as an initial estimate. If the minimum distance found was less than the sum of the stars' radii, a collision was flagged and sent to the collision processing routine (cf. Appendix B).

To verify that the collision finder was working properly, tests were done with full scale clusters ($N_{\rm DC} > 100$) similar to those used in the actual simulations in which numerous randomly selected pairs of stars were given initial conditions that put them on a collision course at a known time and place in the future, normally many orbital periods ahead. The false rejection rate was then found by counting the number of collisions missed by the collision finder; the accuracy of the recovered collision coordinates and minimum distance was also checked. In all tests the loss rate was $< 2\%$, with $\lesssim 1\%$ being the typical case, and the recovered collision parameters were accurate. Additionally, during the production runs histograms of the recovered minimum collision distances (i.e., impact parameters) were tallied and the resulting distributions agreed with that expected from an equal-areas probability law, giving runtime assurance that no bias against the recovery of collisions with any particular impact parameter was being introduced. The rate at which collisions were being found was also examined and found to be consistent with estimates based on the average collision rate determined from the initial distribution function. A foreseen exception is with the outermost stars in this zone, most of whose collision probability is due to stars in the SC region, where these particular DC zone stars spend nearly all of their time. Qualitatively this should not alter the results, since the absolute number of collisions involved with these stars is small; this was confirmed by performing comparison simulations containing only an SC zone, which do not suffer from this problem.

### 3.4. The 'Statistical Collisions' Zone

Conceptually the SC zone is distinguished from the DC zone solely by its method of "finding" the collisions occurring between its $N_{\rm SC}$ stars; in practice this zone contained most of the stars and spanned most of the included volume. Unlike the DC zone, the SC region possesses a fixed outer boundary, $r_{\rm SC}$ ($\ll a_{\rm max}$), which was defined to be the radius at which the initial number of stellar orbits passing within $r_{\rm SC}$ was $N_{\rm SC}$.

The treatment of collisions in the SC region proceeded as follows. At the beginning of each iteration—one iteration being the time interval covered by a single DC stack frame (§ 3.3)—the orbit-averaged collision depth, $\tau_{\rm coll}$, was computed for each star in the SC zone from the expression

$$\begin{aligned}\tau_{\rm coll} &= 2\int_{a(1-e)}^{a(1+e)} \frac{dt(r)}{t_{\rm coll}(r)} = 2\int_{a(1-e)}^{a(1+e)} \frac{{\rm d}r}{v_r(r)t_{\rm coll}(r)} \\ &= 2a^{3/2}\int_{1-e}^{1+e} \frac{\bar{n}_\star(ax,\theta(ax))\langle\sigma_{\rm coll}(v_{\rm rel})v_{\rm rel}\rangle x\,{\rm d}x}{[(1+e-x)(x-1+e)]^{1/2}},\end{aligned} \tag{9}$$

where $v_r^2(r) = [a(1+e)-r][r-a(1-e)]/(r^2 a)$ is the radial component of the star's orbital velocity, $\sigma_{\rm coll}(v_{\rm rel}) = \pi(R_\star + R)^2(1+v_{\rm esc}^2/v_{\rm rel}^2)$ is the cross section for the given star (of radius $R_\star$ and surface escape velocity $v_{\rm esc}$) to collide with one of radius $R$ at relative velocity $v_{\rm rel}$, and $\bar{n}_\star(r,\theta)\langle\sigma_{\rm coll}(v_{\rm rel})v_{\rm rel}\rangle$ is the local collision rate for *that particular* star's orbit, averaged over the current cluster distribution function. We remark that although gravitational focusing has been included in the collision cross-section (since there was no expense in doing so), only rarely will it noticeably enhance the collision probabilities in these simulations (for which $v_{\rm esc}^2/v_{\rm rel}^2 \approx 2\times10^{-6} r_{\rm coll} \lesssim 0.02$). Note also that $\tau_{\rm coll}$ implicitly depends on both the orbital elements of the star and the distribution function of the cluster.

The determination of $\bar{n}_\star$ and the averaging procedure require explanation. Since the integral for $\tau_{\rm coll}$ is being computed every iteration for each of $N_{\rm SC}\sim10^4$ stars, the values of $\bar{n}_\star$ and $\langle\sigma_{\rm coll}(v_{\rm rel})v_{\rm rel}\rangle$—the latter quantity requiring a multi-dimensional integration over the distribution function to find the proper average—needed to be economically calculable. To compute the mean cluster density $\bar{n}_\star = \bar{n}_\star(r,\theta)$ (axisymmetry of the cluster was assumed), a 2-dimensional grid spanning the relevant decades of radius and range of $\theta$ was created anew every iteration, and by computing the fraction of time that each of the $N_{\rm SC}$ stars occupied the discrete bins, the average occupation of each bin (which could thus be $\ll 1$)—i.e., the average number density—was found. Although the average occupation was calculated assuming the orbits were Newtonian, because the mean occupation in $r-\theta$ space depends on the argument of periapse $\omega$ and because the amount of relativistic precession (change in $\omega$) suffered was typically $\sim 0.1-1$ rad per orbit, the average occupation was itself computed as the average of the mean occupations for $\omega = 0$ and $\omega = \pi/2$ (any two orthogonal directions would have been adequate). A proper averaging requires integration over $\omega$ and would have been prohibitive, but as the mean occupation was normally found to vary by at most a factor of two between $\omega = 0$ and $\omega = \pi/2$, averaging the two was satisfactory for present purposes.

The mean density obtained by this procedure is only accurate for $r < r_{\rm SC}$. To compute the mean density at larger radii, a least-squares fit to the distribution function given in equation (7) was done on the stars in the SC zone to estimate the current effective values of $n$, $p$, and $q$, and by matching the easily calculated density of the resulting model to the actual density at $r_{\rm SC}$, the profile for larger radii was obtained.

The value of $\langle\sigma_{\rm coll}(v_{\rm rel})v_{\rm rel}\rangle$ was approximated by

$$\langle\sigma_{\rm coll}(v_{\rm rel})v_{\rm rel}\rangle \approx \pi\langle(R_\star + R)^2\rangle(\langle v_{\rm rel}\rangle + v_{\rm esc}^2/\langle v_{\rm rel}\rangle), \tag{10}$$

which in tests was found to be accurate to $\lesssim 10\%$. The value of $\langle(R_\star + R)^2\rangle$ was found by direct averaging over the stars in the SC region. Computation of $\langle v_{\rm rel}\rangle(r)$ was done by first defining $g_{\rm coll}(r) = \langle v_{\rm rel}\rangle(r)/v_{\rm orb}(r)$ and then pre-computing a (5-dimensional!) table of values $A$ and $B$ such that $g_{\rm coll}(r) \approx A + Br$, depending on $a$, $e$, $i$, $p$ (the velocity space anisotropy parameter), and $q$ (the real space anisotropy parameter); dependence on $n$, the power law index for the density, was extremely weak and was neglected. The values of $A$ and $B$ for the given star were then interpolated from this table, allowing very efficient calculation of $\langle\sigma_{\rm coll}(v_{\rm rel})v_{\rm rel}\rangle$. Much of the preceding, rather elaborate procedure was done to allow reasonably accurate computation of $\tau_{\rm coll}$ even for highly anisotropic clusters.

Comparison of the values for $\tau_{\rm coll}$ computed by this run-time procedure with accurate routines which explicitly performed the multi-dimensional integrals for each individual case showed the above procedure to have typical errors of $\sim 10-20\%$, with very few values off by more than 50%; this was deemed quite acceptable, particularly since $\tau_{\rm coll}$ affects only the *rate* at which collisions were made to occur, not the circumstances or outcomes of those collisions. By way of analogy, if one thinks of the dynamical evolution of the stars in the SC zone as a movie, then the value of $\tau_{\rm coll}$ doesn't alter the movie's ending, only whether it plays at normal speed, in slow motion (if $\tau_{\rm coll}$ is underestimated), or in fast forward (if $\tau_{\rm coll}$ is overestimated).

After computing the value of $\tau_{\rm coll}$ for a particular star, the star was given the opportunity to suffer a collision that iteration with probability $1 - \exp[-\tau_{\rm coll}]$. The result of doing this for all stars was a list of stars that were to suffer a collision that iteration, which were then randomly paired off with each other and set up to collide by suitably altering the orbital elements $\omega$ and $\Upsilon$ for each, with the radius of the collision point being randomly drawn from a probability distribution properly weighted by the input density profile. By construction the impact parameters of these collisions follow an equal-areas law. When matching collision partners it was required that the two stars' orbits overlap radially, ensuring that a collision was physically reasonable. Occasionally this procedure produced 'widow' stars for which no suitable collision partner was present in the list (they were a minor fraction of the total; note however that widows are unavoidable since the total number of stars in the list need not be even); in this case, either the star was removed from the list and given a reprieve, or the cluster star with the largest $\tau_{\rm coll}$ whose orbit overlapped that of the widow's was added to the list and paired with it (which option to take was determined randomly, with each being equally probable so as not to bias the average collision rate.) Comparative simulations in which widows were always removed from the list performed similarly. Subsequent treatment of the collisions was handled identically as for ones found by the collision finding algorithm.

The results of the simulations indicate that the above procedure produced collisions nearly indistinguishable from ones which would have been found by the collision finder, as judged by the smooth transition between the two regions and the similarity of the histograms describing the circumstances and outcomes of the collisions. This afforded confidence in doing simulations lacking a DC zone entirely, allowing a considerably greater number of models to be examined. Repeating a simulation with and without a DC zone also allowed the significance of the loss in collision probability for the outer DC stars (mentioned in the previous section) to be estimated. Since in absolute terms the number of collisions occurring in the SC region was considerably larger than in the DC region, this loss of probability was not found to alter the results noticeably. Complete results are given in § 4.

### 3.5. The Reservoir

The 'reservoir' consists of all stars present in the initial distribution function but not explicitly included in the simulations, i.e., all stars with periapses greater than $r_{\rm SC}$. The dynamical evolution of these stars is not considered here; owing to the longer timescales involved at greater distances, this evolution would not be substantial in any event. However, relaxation processes in the outer cluster will lead to the occasional injection of a star into the inner core that *is* being treated numerically, and to reach a steady state solution this process must be taken into account. On the other hand, there are plausible circumstances under which a one time injection of stars could occur, such as the tidal disruption of a globular cluster or dwarf spheroidal passing close to a larger galactic nucleus, in which the stars would be slowly consumed without replenishment. To examine this latter case, some of the runs did not include the reservoir at all but instead allowed the cluster to slowly deplete itself until densities dropped to such a level that collision timescales became very long. For the simulations in which it was desired to reach a steady state, the injection of stars by the reservoir was treated as follows.

By Jean's Theorem, since $\mathcal{E}$, $L$, and $L_z$ are all conserved in a $1/r$ potential (as well as in the Kerr geometry, with suitable identification of the integrals of motion), any distribution function of the form $f = f(\mathcal{E}, L, L_z)$ is a solution of Vlasov's Equation and describes a valid equilibrium state, assuming relaxation is the dominant dynamical process. In equilibrium, the rates of relaxation into and out of an orbit of given $a, e$, and $i$ must be the same, so that the distribution of orbital parameters is time-independent. Hence the parameters of those reservoir orbits which have relaxed so as to bring them inside $r_{\rm SC}$ must follow the same distribution as the orbits already inside $r_{\rm SC}$, and the orbital elements of each star injected can be found by the same procedure used to set up the initial cluster (see § 3.1). What remains to be computed is the rate at which these stars should be added to the inner cluster. To estimate this, recall that the relaxation time for a star on a given orbit can be thought of as the timescale on which the orbit's mean square angular momentum changes by $L^2_{\rm max}(\mathcal{E}) = 1/(2\mathcal{E}) = a$ (e.g., Lightman & Shapiro 1977). For a star with given $a$ and $e$ such that $a(1-e) > r_{\rm SC}$, we want to know the average length of time it will take for this star to diffuse onto an orbit with $a'(1-e') < r_{\rm SC}$; by then averaging over all relevant $a$ and $e$ using the distribution function, the net rate at which stars should be added will be found. The rate of change of $L^2$ can be written

$$\frac{{\rm d}(L^2)}{{\rm d}t} \sim \frac{L^2_{\rm max}}{t_{\rm r}} = \frac{\tau_{\rm r}}{2\pi a^{1/2}}, \tag{11}$$

where the orbit-averaged, dimensionless relaxation depth $\tau_{\rm r}$ is given by

$$\tau_{\rm r}(a,e) = 2\int_{a(1-e)}^{a(1+e)} \frac{{\rm d}t(r)}{t_{\rm r}(r)} = 2\int_{a(1-e)}^{a(1+e)} \frac{dr}{v_r(r)t_{\rm r}(r)}, \tag{12}$$

where $t_{\rm r}(r) \sim v^3_{\rm orb}(r)/[15G^2m^2_\star n_\star(r)\ln(0.4N_\star)]$, $v^2_{\rm orb} = 2/r - 1/a$ (the star's orbital speed), and $v_r^2 = [a(1+e)-r][r-a(1-e)]/(r^2a)$ (the radial component of $v_{\rm orb}$). Now the given orbit will diffuse into the region $r < r_{\rm SC}$ when the condition $L^2 < L^2_{\rm min} = a(1-e^2_{\rm min})$ is met, where $a(1-e_{\rm min}) = r_{\rm SC}$. The amount of time this takes is $\Delta t(a,e) \sim [(L-L_{\rm min})/L_{\rm max}]^2 t_{\rm r}$. The distribution function was used to average this result over the reservoir to derive the net injection rate. For $n = 7/4$, $p = q = 0$, $n_\star(1\,{\rm pc}) = 10^6 n_6$ pc$^{-3}$, and $M = 10^8 M_8\, M_\odot$, the numerical value of this injection timescale is

$$t_{\rm inj} \approx 5000 M_8^{7/4} n_6^{-1} \left(\frac{m_\star}{M_\odot}\right)^{-2} \left(\frac{N_\star}{10^6}\right)^{-1} \ {\rm yr}, \tag{13}$$

and is a slowly increasing function of $p$. For solar mass stars, note that this implies an average mass injection rate of $\sim 10^{-3} M_\odot$ yr$^{-1}$ for typical simulation parameter values; this is comparable to the accretion rate required to power a moderately luminous Seyfert galaxy.

## 4. Simulation Results and Discussion

Numerical results will be presented in a series of four fiducial models covering a range of black hole masses, cluster densities, and initial mass functions. The parameters for each

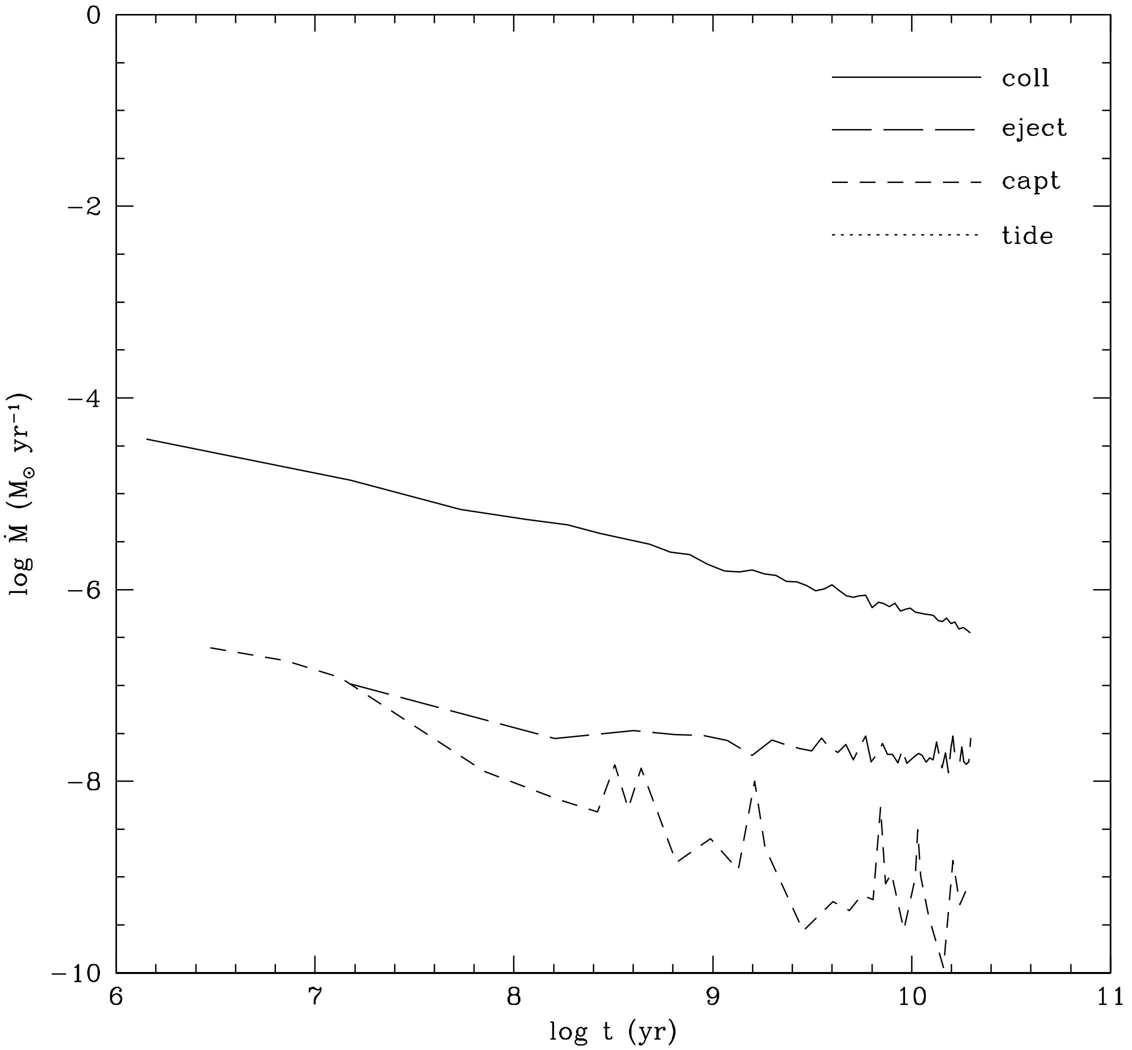


Fig. 1.— Cluster mass depletion rates for model 1 (see Table 2) due to collisions, tidal disruption, and post-collision stars whose orbits are either captured by the hole or unbound (ejected) with respect to it. In this case there is no tidal mass loss since since the tidal radius lies inside the horizon.

model, listed in Table 2, are: the mass of the black hole, $M_8 = M/(10^8 M_\odot)$; the velocity anisotropy parameter of the initial cluster, $p$ (see § 3.1); the stellar initial mass function, $f(m)$; the density scale, $\rho_6 = \rho_\star(1\ \mathrm{pc})/(10^6 M_\odot\ \mathrm{pc}^{-3})$; the initial number of stars in the simulation, $N_{\rm SC}$; and whether the model included an outer reservoir (§ 3.5). The models with $f(m) \propto \delta(m - M_\odot)$ initially contain a cluster of identical, solar mass stars; the clusters with $f(m) \propto m^{-2.35}$ assumed a Salpeter mass function over the interval $[0.4, 4.0]\ M_\odot$, which implies an average stellar mass of $\approx 0.9 M_\odot$. In addition, all initial clusters were spherically symmetric (flattening parameter $q = 0$) with input densities $\rho_\star(r) \propto r^{-7/4}$. All models presented here used $j = 1$ for the spin of the MBH; comparison models computed using $j = 0$ showed no perceptible difference from the corresponding $j = 1$ model and are not shown (see also § 5). Finally, we note that none of the fiducial models included a DC zone (§ 3.3); such simulations are much more demanding computationally, which severely limits their relative radial and temporal dynamic range. Complementary simulations using the DC algorithm exhibited the same qualitative evolution as the fiducial models and showed that the performance of the SC routines (§ 3.4) was nearly identical to that of the DC algorithm. The following subsections discuss the results of the single injection (no reservoir) models and steady state (reservoir included) models, respectively.

For each fiducial model, a set of three comparison models was run in which either $N_{\rm SC}$ was reduced by a factor of 3, $p$ was changed, or the SPH fitting formulae were replaced with the trivial rule that all collisions resulted in the total disruption of both stars. These additional runs served as controls allowing sensitivity to the corresponding parameters to be estimated. It was found that reducing $N_{\rm SC}$ (and thus the completeness limit, $r_{\rm SC}$) did not qualitatively change any results; it simply reduced the total collision rate—by roughly 20% for each halving of the simulation volume—due to the increased incompleteness. As the collisions are highly centrally concentrated, even less change would be expected had larger

Table 2. Fiducial Simulation Parameters

| Model | $M_8$ | $p$ | $f(m)$ | $\rho_6$ | $N_{\rm SC}$ | Reservoir? |
|---|---|---|---|---|---|---|
| 1 | 10 | 10 | $\propto \delta(m - M_\odot)$ | 0.03 | $3 \times 10^4$ | no |
| 2 | 0.3 | 0 | $\propto m^{-2.35}$, $0.4 \le m/M_\odot \le 4$ | 0.3 | $1 \times 10^5$ | no |
| 3 | 0.01 | 0 | $\propto m^{-2.35}$, $0.4 \le m/M_\odot \le 4$ | 0.3 | $3 \times 10^4$ | yes |
| 4 | 0.3 | 5 | $\propto \delta(m - M_\odot)$ | 0.1 | $3 \times 10^4$ | yes |

numbers of stars been used. Dependence on the remaining factors is discussed along with the main results.

### 4.1. Single Injection Models

Models 1 and 2 did not include a reservoir, and hence display continually decreasing densities and collision rates. These models could correspond to a sudden influx of stars to the nucleus from a tidally disrupted globular or a close interaction with another galaxy, which is afterwards gradually depleted through collisions and consumption by the black hole. They are also useful as a reference for comparison with the steady state models, which include injection of new stars from an extended outer cluster (§ 4.2). The output quantities for each model include the mass loss rates into several modes, the density profile, and the stellar mass spectrum; another useful diagnostic shown for model 2 is the evolving eccentricity distribution.

The results for model 1 are given in Figs. 1-3. This model consists of a $10^9 M_\odot$ black hole and a relatively low density cluster with moderate anisotropy (tangential bias)—parameters qualitatively similar to those of M87, for example. Figure 1 shows the mass release rates as a function of time into four different channels: collisional, tidal, captured, and ejected. The collisional mass loss is simply the total amount of gas directly unbound from colliding stars. As this mass is normally ejected at high velocity and at random angles to the radial direction, roughly half of it will remain bound to the hole and half will be ejected from the core; in all simulations this mass loss rate was also the largest of the four, usually by factors of a few. The tidal mass loss rate contains the mass of all tidally disrupted stars, about half of which will be accreted by the black hole (cf. §3.2). In the single injection models tidal disruption is due solely to stars deflected into the loss cone after colliding with another star ("collisional refilling of the loss cone"); for the models including a reservoir, limited relaxation-driven refilling of the loss cone is also present. The captured mass rate results from stars whose post-collision orbits have so little angular momentum that they cross the horizon and are consumed; this mass is closely related to the tidal mass loss, the main difference being that essentially all of the captured mass will plunge directly into the hole (with minimal energy release), whereas in the latter case the bound mass (roughly half of the total) will accrete slowly with much higher radiative efficiency. The ejected mass rate is due to stars whose post-collision orbits are no longer bound to the hole; these stars are ejected from the (inner) core in a dynamical time. The pattern in Fig. 1 was typical, with collisional mass release being largest, followed by ejected mass, tidal mass loss, and mass loss by direct capture. (The 'tidal' curve is not present in Fig. 1 because the tidal radius was inside the horizon for

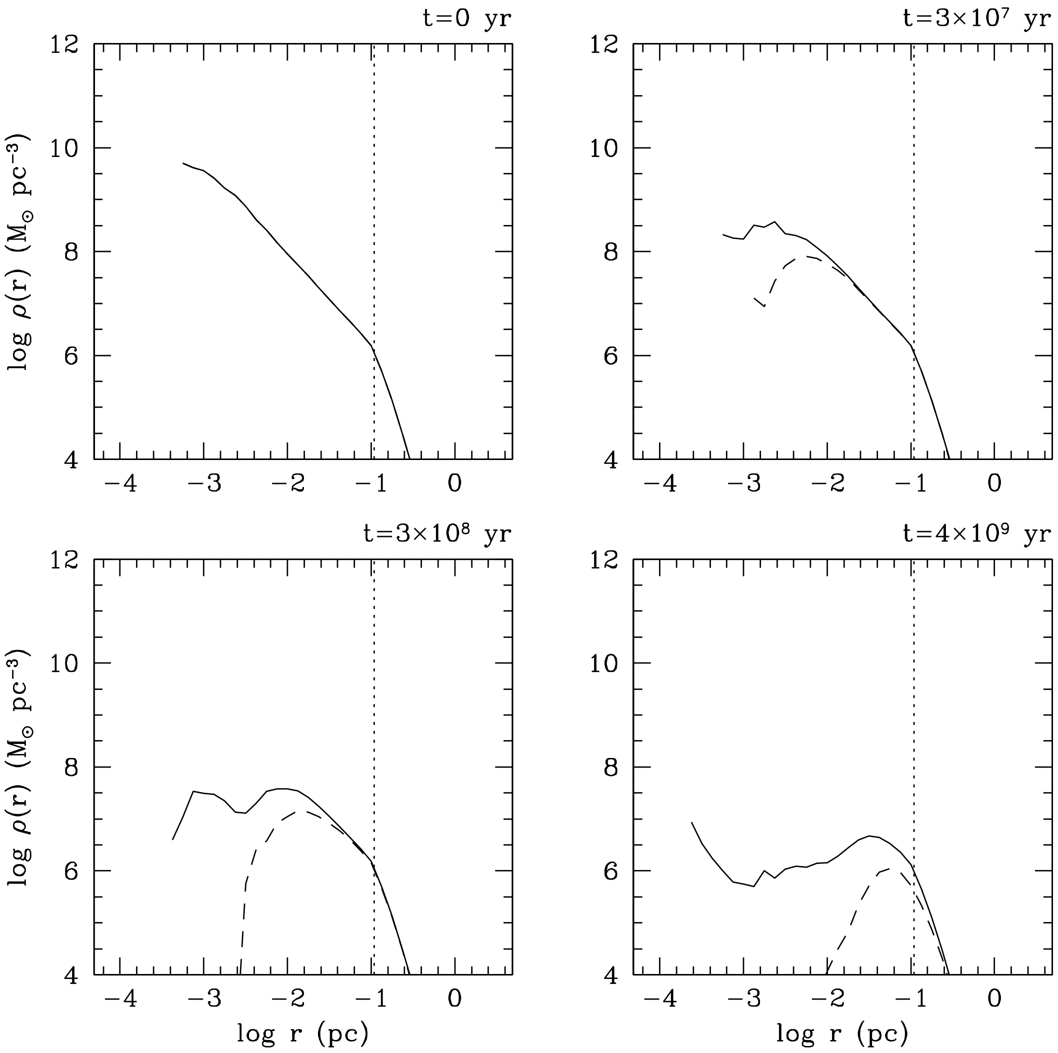


Fig. 2.— The density of cluster model 1 at several epochs. The solid curves are the results assuming realistic collision products; the dashed curves result from assuming that collisions completely disrupt both stars. The dotted line denotes the value of $r_{\rm SC}$, the maximum simulation radius; outside this limit the density is incomplete. Collisions lead to the development of an inner core of nearly constant density (within statistical fluctuations).

this model.)

The evolution of the density in model 1 at several epochs is shown in Fig. 2. The solid curves are the results using the SPH fitting formulae (see Appendix B) to determine collision outcomes; the dashed curves show the results when all collisions are assumed to completely disrupt both stars. When collisions are realistically treated, there is clear evidence for the development of a nearly constant density core, which extends outward to larger radii as time passes. This is in direct contrast to the results of Fokker-Planck calculations (see § 1), which find $r^{-1/2}$ cusps in the collision-dominated region. The Fokker-Planck scaling can be easily explained as follows. Consider an isotropic cluster with distribution function $f(\mathcal{E})$, where $f(\mathcal{E}) \sim 0$ when $\mathcal{E} > \mathcal{E}_0$. The density $\rho(r)$ in this case is

$$\rho(r) = \int f(\mathcal{E})\,\mathrm{d}^3\boldsymbol{v} = 4\pi \int f(\mathcal{E}) v^2\,\mathrm{d}v = 2^{5/2}\pi \int^{\mathcal{E}_0} f(\mathcal{E}) \left(\frac{1}{r} - \mathcal{E}\right)^{1/2} \mathrm{d}\mathcal{E}, \tag{14}$$

where $\mathcal{E} = 1/r - v^2/2$ has been used; for $r \ll a_0 = 1/(2\mathcal{E}_0)$, $(1/r - \mathcal{E})^{1/2} \approx r^{-1/2}$ and one therefore finds $\rho(r) \propto r^{-1/2}$. (Small amounts of anisotropy do not alter this result; for the distribution (7) with $p = 5$, e.g., the cusp profile is $\approx -0.3$ for $r \sim 0.1a_{\rm min}$ and $\approx -0.48$ for $r \sim 0.01a_{\rm min}$; in Fig. 2, the weak cusp to be expected at small radii is either below the axis or—more likely—truncated due to discreteness effects and the finite horizon radius.) Previous studies have assumed complete disruption of stars at the velocities present in these simulations (typical collision velocities were $\gtrsim 3000$ km s$^{-1}$), and hence created such cusp-producing $f(\mathcal{E})$ when the most tightly bound stars collided and were subsequently removed from the simulations. In the present (anisotropic) case, the very weak cusp which would emerge at small radii is not visible on the scale of the plots, and hence assuming totally disruptive collisions results in a rapidly decreasing density at small radii. Examination of the distribution of semi-major axes for model 1 confirmed that a modest but non-negligible tail of low-$a$ stars—made up of the low mass collision fragments (see the following paragraph)—persisted even at late times in the simulation incorporating realistic collisions. Such a tail can dominate the local density, burying beneath it the weak $r^{-1/2}$ cusp produced by large-$a$ stars, and this is what is happening in this case; the creation of a small tangential bias in the turnover region is also implied, which is intuitive since (for fixed $a$) stars with slightly larger $e$ (i.e., smaller $r_{\rm min}$) have slightly higher collision frequencies. The Fokker-Planck results thus appear to be an artifact of their oversimplified treatment of the collision dynamics (and in most cases, their assumption of isotropy), which the present simulations follow much more accurately.

Figure 3 displays the evolution of the mass spectrum. In single injection models the mass spectrum will be substantially altered when most stars have had an opportunity to collide; for steady state models the addition of new stars stabilizes this process, as discussed in § 4.2.

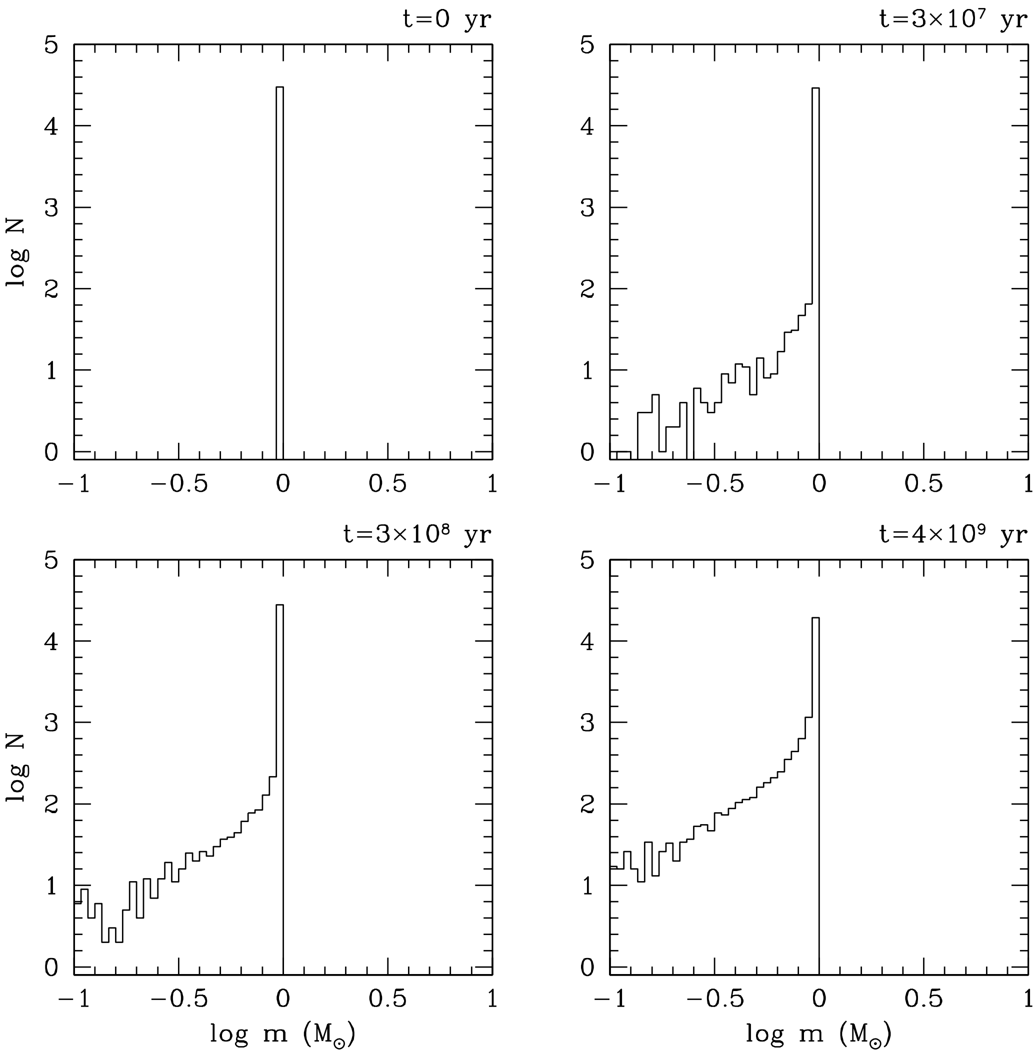


Fig. 3.— The mass function of cluster stars at several times for model 1. A significant tail of low-mass collision fragments develops by late times.

In model 1 approximately half of the stars had disrupted at the end of the simulation; as seen in Fig. 3, collisions produce a significant tail of low mass stars, even though nearly all collisions occurred in the 'disruptive' regime. Physically this occurs because most of the collision cross-section is at large impact parameters, and since the mass of typical main-sequence stars is rather centrally concentrated, these collisions produce relatively little mass loss even at very high speeds—highlighting the uncertainty of simulations which assume complete disruption under these conditions.

Examination of the distribution of orbital eccentricities at several epochs (not shown) revealed no discernible evolution, even though $\sim 30\%$ of the original stars had disrupted by $t = 4 \times 10^9$ yr. This is somewhat surprising, since orbits with large $a$ have systematically larger $e$ (a result of all stars initially satisfying $a(1-e) < r_{\rm SC}$); thus progressive removal of the shortest period (smallest $a$) orbits should generically lead to an increasing radial bias in the remaining stars (cf. Fig. 7). The result can be explained by noting that the tangential velocity bias present in the initial cluster significantly reduces the typical eccentricity of the stellar orbits; this implies that $r_{\rm min}$ (which determines the collision depth per orbit—cf. eq. [1]) varies relatively little among stars with similar $a$. Collision timescales should therefore be insensitive to $e$ in this case, in agreement with the numerical results.

Similar plots of the distribution of orbital inclinations showed no statistically meaningful deviations from spherical symmetry; the same was true of *all* models computed during the course of this work. There is thus no evidence that the anisotropy of the Kerr spacetime leaves any noticeable imprint on the cluster distribution function; further discussion of this issue is given in § 5.

Figures 4-7 show the results for model 2, and are analogous to Figs. 1-3. This model consisted of an 'AGN-class' black hole of mass $3 \times 10^7 M_\odot$ surrounded by an isotropic, moderately dense cluster of stars having a range of initial masses. Fig. 4, which plots the mass loss rates, is qualitatively similar to Fig. 1; the more rapid drop in the curves at lates times is due to the near-total depletion of the initial cluster at that point. Asymptotically the rates scale approximately $\propto t^{-1}$. The results for the density evolution are shown in Fig. 5. As is clearly seen in the figure, the $r^{-1/2}$ cusp which would have been found had collisions been assumed to be totally disruptive (dashed curves) is hidden below the relatively flat core resulting from a realistic treatment of collisions (solid curves). Another general feature seen here is the tendency for an increased level of Poissonian fluctuations relative to the tangentially biased models (cf. Fig. 2); this is a consequence of the greater range of orbital energies that contribute to the density at a given radius in isotropic models.

Figure 6 displays the corresponding mass function evolution. In this model the low-mass tail is partially hidden by the main distribution; at late times, however, it and the relative

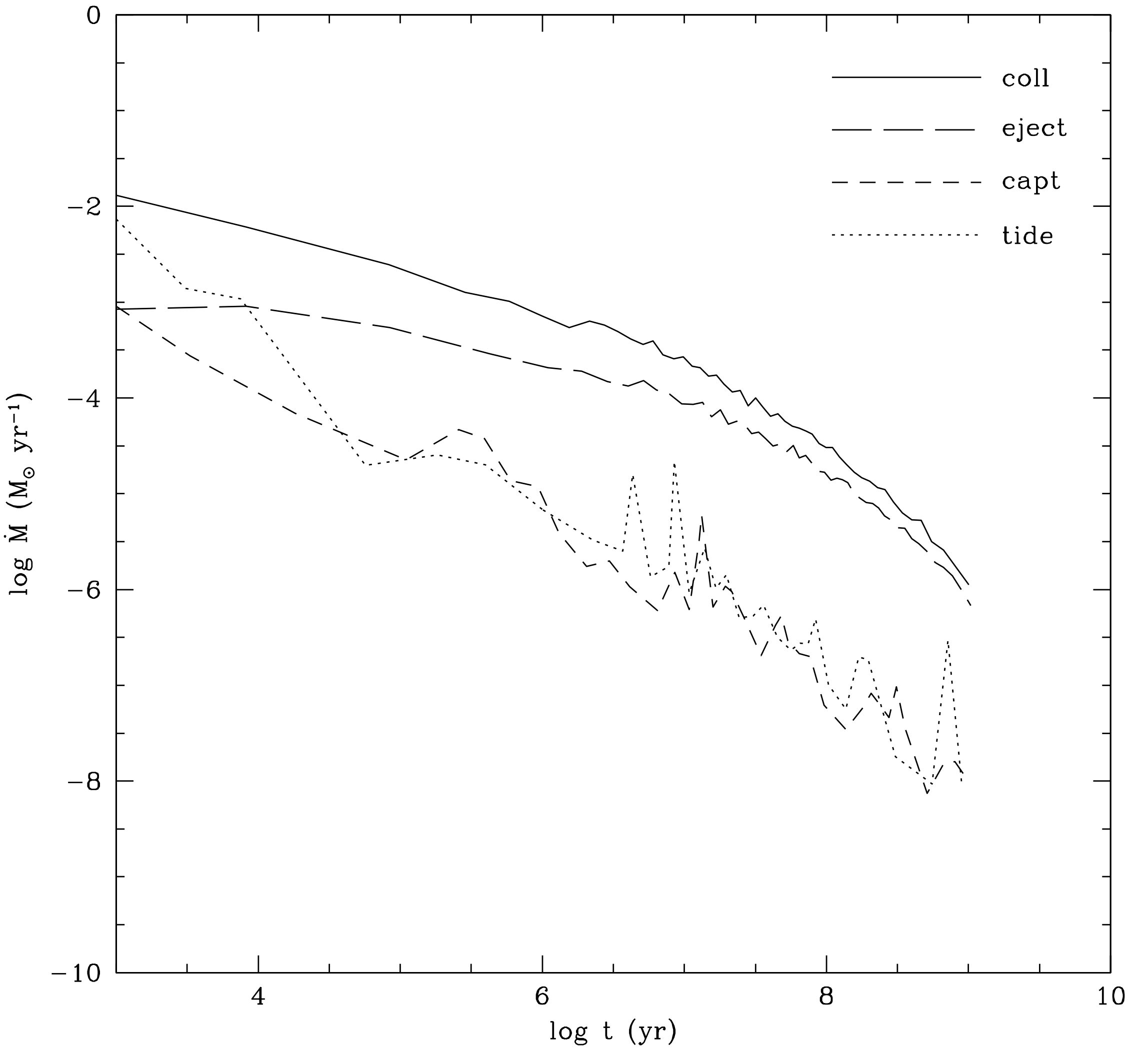


Fig. 4.— Mass loss rates for model 2. At late times this cluster was nearly devoid of stars, leading to an accelerating decline in the mass rates.

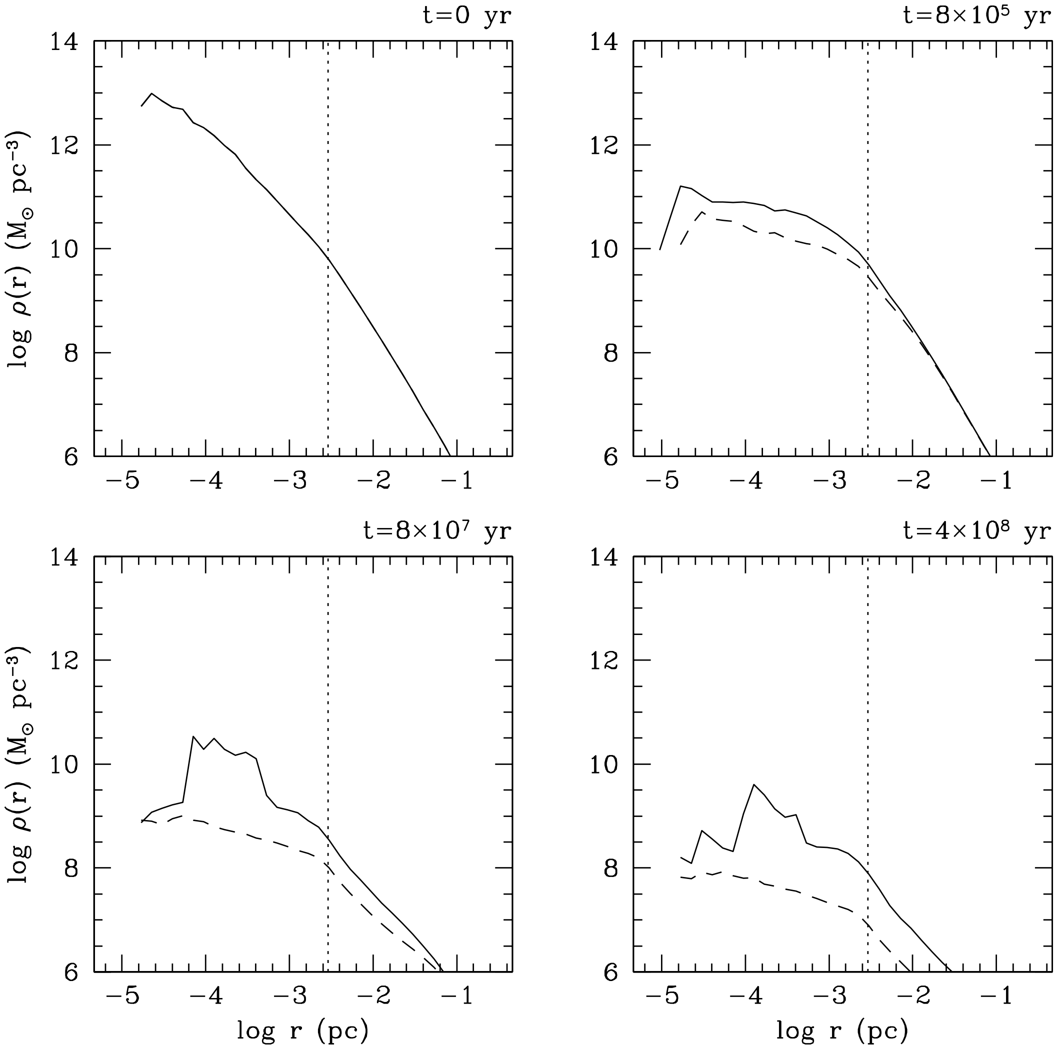


Fig. 5.— Evolution of the density in model 2. The simulation incorporating realistic collision products (solid curves) produces a relatively flat core (subject to Poissonian fluctuations) that overshadows the weaker $r^{-1/2}$ cusp that results if collisions are assumed to be completely disruptive (dashed lines).

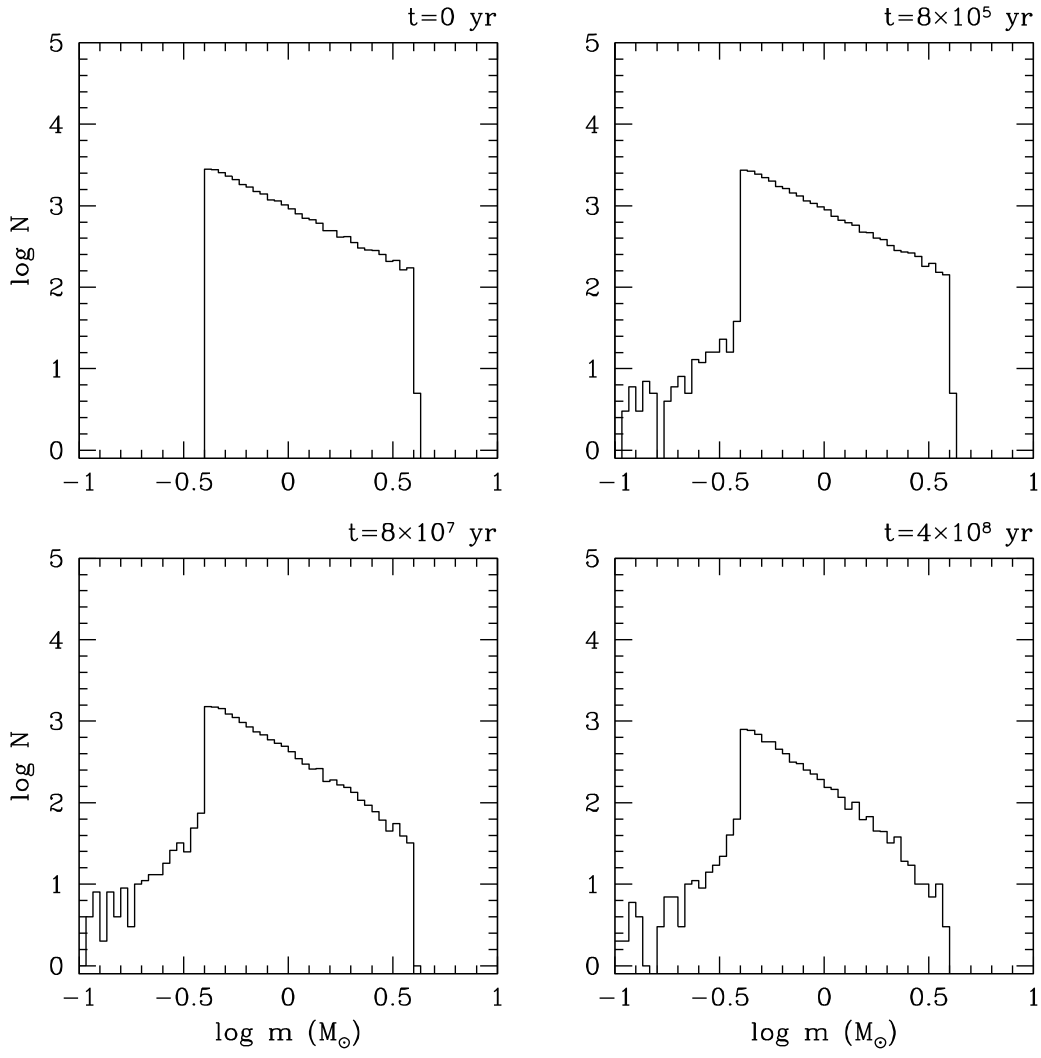


Fig. 6.— Evolution of the stellar mass function for model 2. The larger geometric cross-section of high mass stars leads to their depletion relative to other stars, with post-collision stellar fragments creating an excess of low-mass stars.

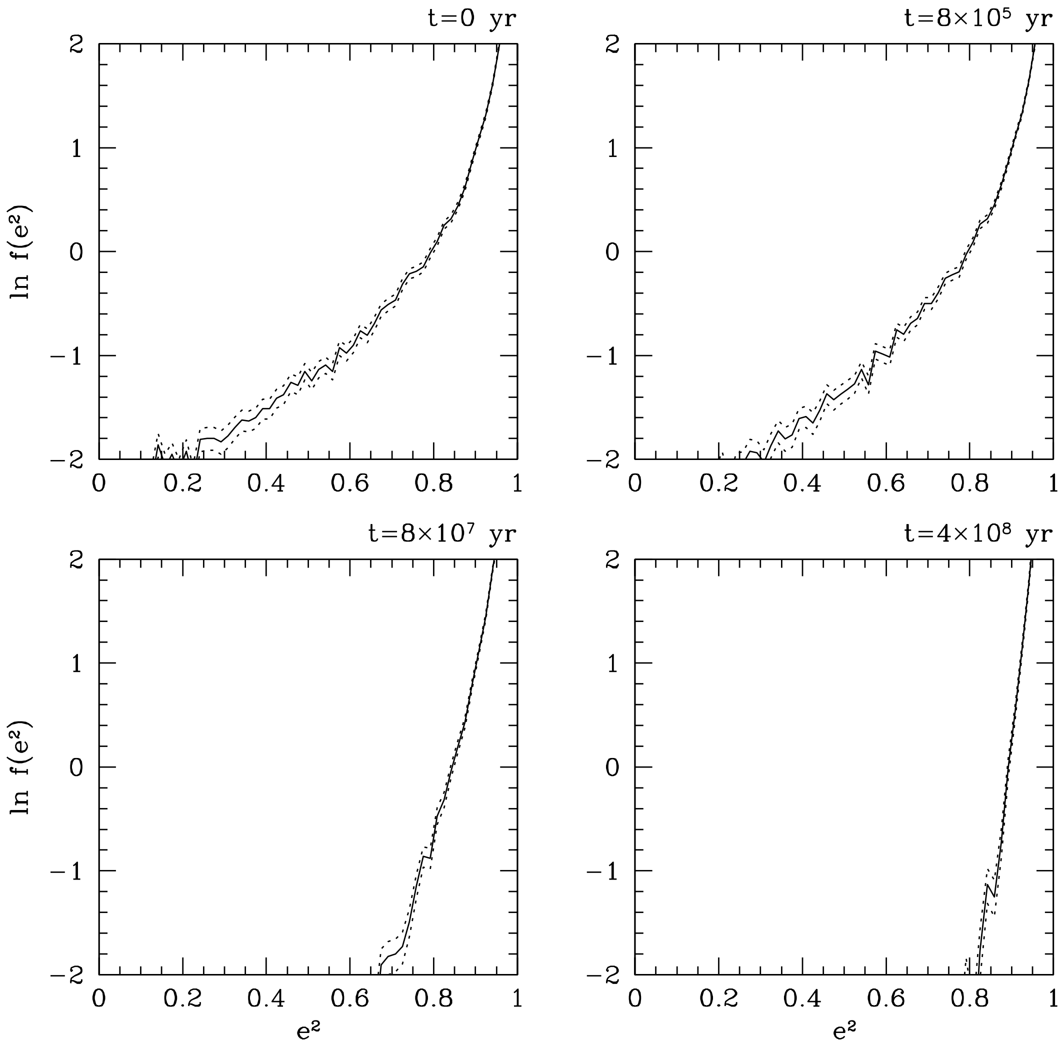


Fig. 7.— The normalized eccentricity distribution of stars in model 2 (the dotted lines are estimated $1-\sigma$ error bars). The profile becomes progressively radial since orbits with smaller $e$ (and hence, on average, smaller $a$) tend to have the highest collision frequencies. The initially isotropic ($p = 0$) cluster does not produce a flat line because the stars are heavily biased towards large $e$ by the condition $a(1-e) < r_{\rm SC}$.

depletion of high-mass stars (a consequence of their larger geometric cross-sections) are plain. Note that in this particular case the mass function at late times ($\gtrsim 10^8$ yr, roughly the main sequence lifetime of a $4M_\odot$ star) will also be affected by stellar evolution, which has been neglected here. Besides the eventual removal of high mass stars that have evolved into white dwarfs or neutron stars, the greatly increased cross-sections of giant branch stars will also considerably decrease their collision timescales. On the other hand, since the extended outer envelopes of such stars consist of relatively low-density, loosely bound material, collisions involving such stars are unlikely to be fully disruptive or to liberate large amounts of mass; in addition, approximately 95% of the cluster stars had lifetimes exceeding the length of the simulation. For this reason the inclusion of stellar evolution effects would not have significantly affected the final results, aside from truncating the final mass function above $\sim 2.5M_\odot$ and introducing a new mass loss channel associated with outflows/stellar remnant formation (the fate of which is beyond the scope of this paper).

Finally, Fig. 7 shows the evolving eccentricity distribution. Here the increasing radial bias over time is prominent and occurs for precisely the reason mentioned above—i.e., because in this model the eccentricities of most small-$a$ stars are smaller than the average, so their systematic removal engenders an apparent radial bias in the inner core.

### 4.2. Steady State Models

Although the relaxation timescale is much longer than the collision time within the simulation volume, relaxation will occasionally cause some stars in the outer core to lose enough angular momentum that they subsequently enter the SC zone near periapse; these stars will then support a quasi-steady state stellar distribution in the inner core. The way this process was modeled in these calculations was described in § 3.5. Models 3 and 4 provide two examples of the results of this procedure.

Figures 8 and 9 show the results for model 3, which contained a $10^6 M_\odot$ black hole in an isotropic cluster of stars having a range of masses; the parameters of this model are broadly similar to those of the Galactic Center. Figure 8 shows the evolving mass loss rates, which are qualitatively similar to those of the previous models except for the initiation of steady state loss rates after $\sim 10^7$ yr; the equilibrium collisional mass loss rate is $\dot{M}_{\rm coll} \approx 5{\times}10^{-4} M_\odot$ yr$^{-1}$. (In reality these curves would continue to slowly decrease as the outer core depleted itself, but the effect will only be important over a relaxation time.) Note also the relatively large amount of tidal mass loss, a consequence of the tidal radius lying well outside the horizon in this case ($r_{\rm t} \sim 100$). The density profile is plotted in Figure 9; as in previous models, the cusp produced assuming fully disrupting collisions is hidden beneath the profile resulting

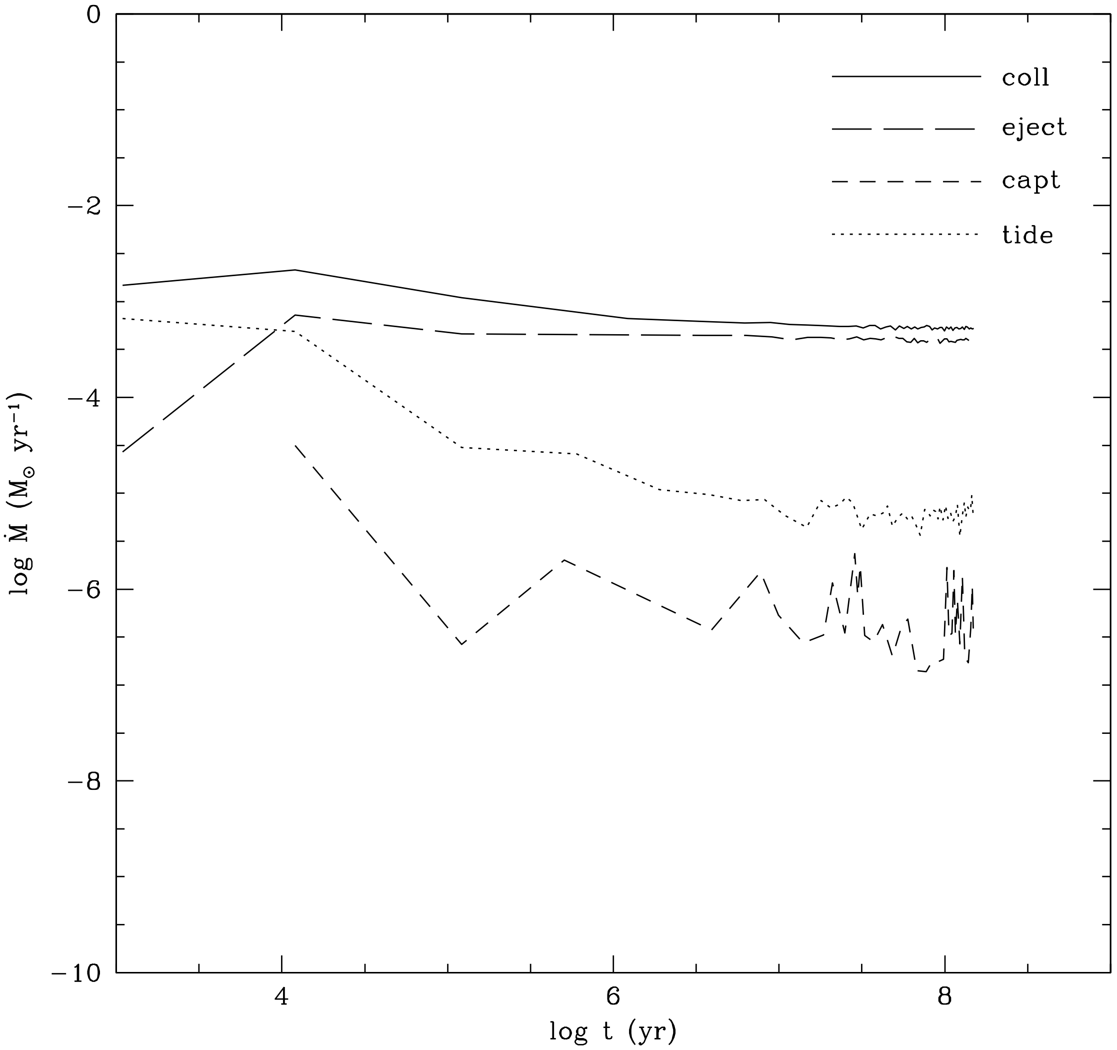


Fig. 8.— Mass loss rates for model 3. The steady state collisional mass loss rate is $\approx 5 \times 10^{-4} M_\odot$ yr$^{-1}$.

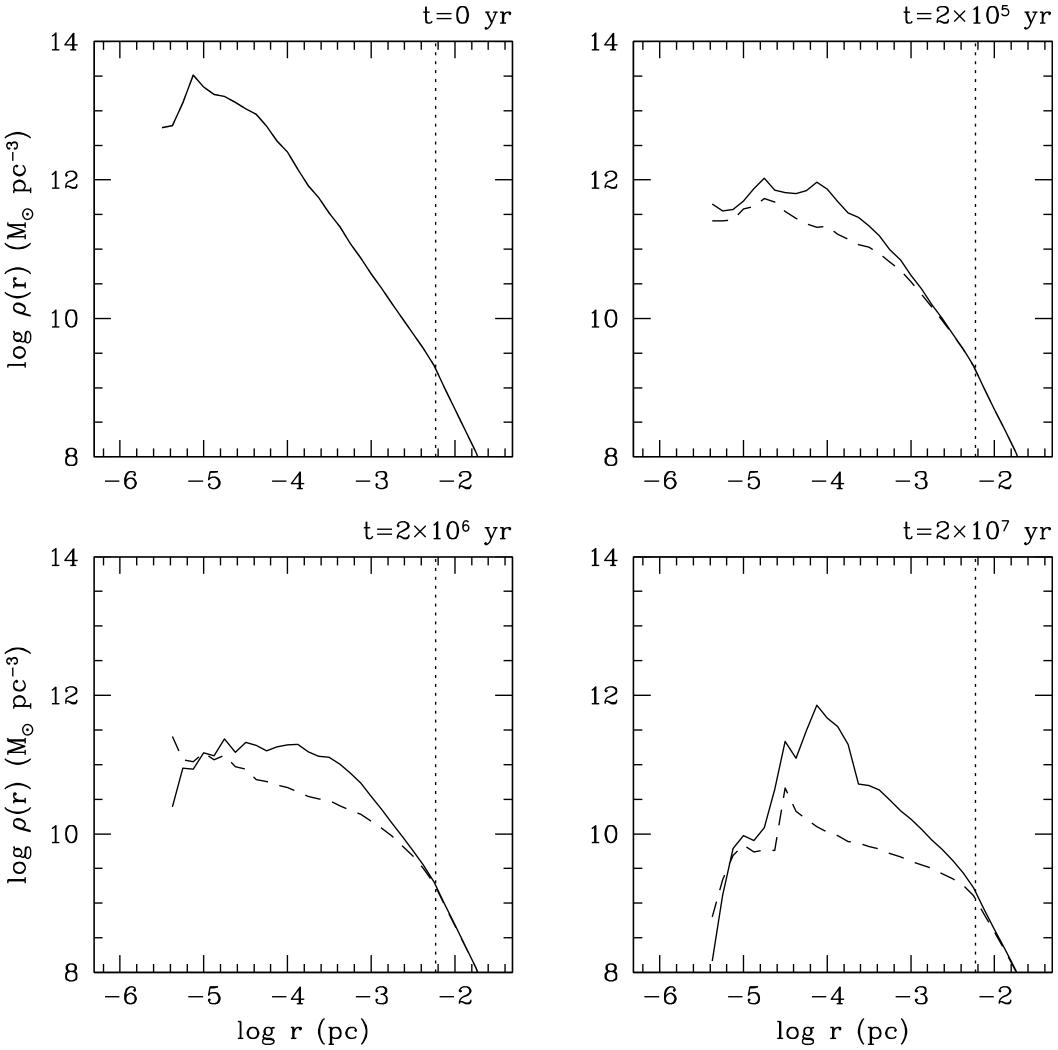


Fig. 9.— Evolution of cluster density for model 3 (cf. Fig. 2). The completeness limit (dotted line) for this model is $r_{\rm sc} \approx 10^5 M \approx 6 \times 10^{-3}$ pc. As before the weak cusp produced assuming totally disruptive collisions (dashed lines) is hidden beneath the density profiles resulting from a more realistic treatment of collisions (solid lines). The qualitative evolution of the mass spectrum in this model was similar to that in Fig. 6, only less pronounced.

from a more realistic treatment of collisions. The mass function evolution (not shown) was qualitatively similar to that in Fig. 6, though the effects were much less pronounced due to the injection of new stars (drawn from the fixed, initial mass distribution), which tends to stabilize the mass function towards its initial value.

Results for model 4 are given in Figures 10 and 11. This model (somewhat similar to model 2) consisted of a $3 \times 10^7 M_\odot$ black hole, a somewhat tangentially biased cluster ($p = 5$), and equal mass stars, and is roughly comparable to nuclei such as that in M31. The mass loss rates are displayed in Fig. 10, and contain nothing qualitatively new; in fact, they show that a steady state had not been reached when the simulation was finally terminated (there is perhaps a hint of stabilization after $10^{10}$ yr). The density evolution (Fig. 11) is also similar to previous models, and a flat (or even slightly decreasing) core is prominent as the evolution proceeds. Mass function evolution was similar to Fig. 3, but again the tail was less pronounced due to stabilization by newly injected stars.

## 5. Conclusions

The principal new result of this study is that physical collisions preferentially produce a flat core in the collisionally dominated region of the cluster, in contrast to the $r^{-1/2}$ cusp found previously in Fokker-Planck studies. The discrepancy can be traced to the highly simplified treatment of collision dynamics and the imposition of isotropy in the Fokker-Planck calculations (their inability to model sparsely populated regions of phase space may also play a role)—limitations from which the simulations described here do not suffer. It was found that grazing collisions created a significant population of bound, low mass collision fragments, even at relative velocities for which a head-on collision would lead to complete disruption. Perhaps most intriguing in this regard are the results of Murphy et al. (1991), who incorporated routines to more realistically estimate the masses of collision products (based on the method of Spitzer & Saslaw 1966) but still obtained cusps close to $r^{-1/2}$. However, by necessity their multi-mass Fokker-Planck code can include only a limited number of discrete stellar masses, which impedes the formation of collision-resistant, low mass remnants in at least two ways. The first is the hard lower limit on stellar mass ($0.3 M_\odot$ in their simulations), which is not present here. The second arises during grazing collisions where the implied mass loss is less than the separation between adjacent mass bins: although bin occupancy will decrease, remnant mass will not. These factors may bias the calculation towards the complete disruption of stars, which in isotropic Fokker-Planck codes guarantees production of $r^{-1/2}$ cusps; a definitive answer to this question is, however, beyond the scope of this paper. In terms of the mass production rates, on the other hand, the findings

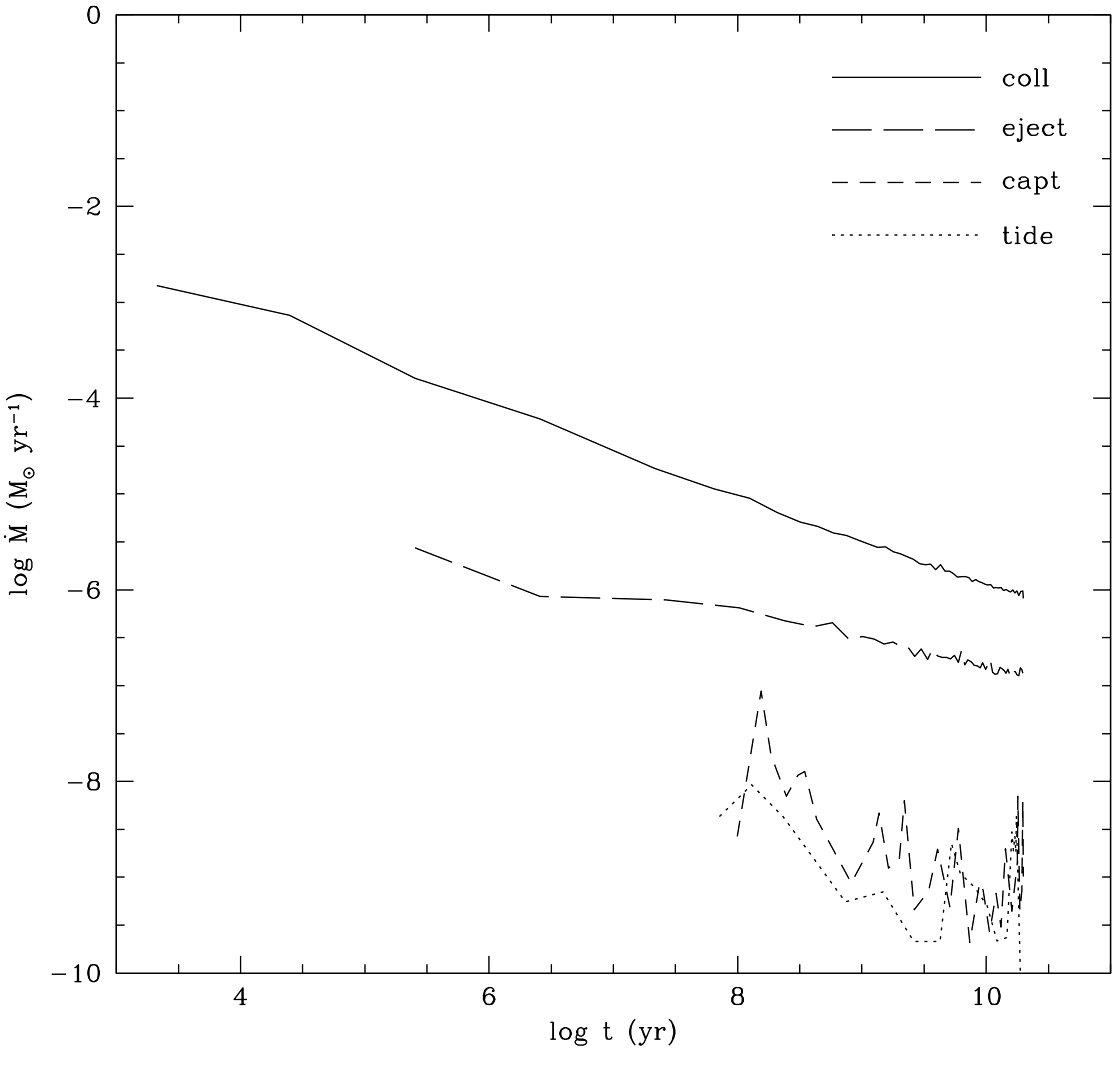


Fig. 10.— Mass loss rates for model 4. In this case a steady state was not reached within $10^{10}$ yr.

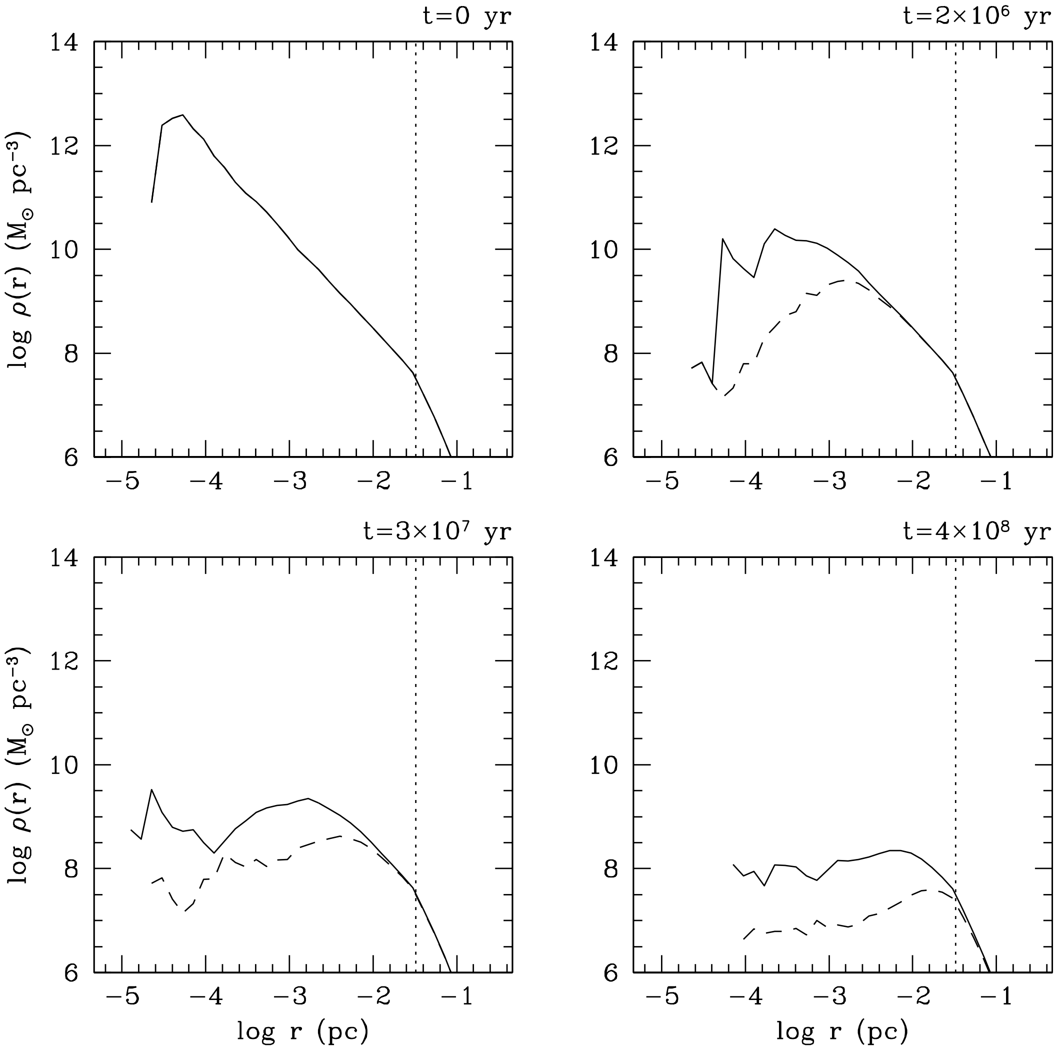


Fig. 11.— Evolution of the stellar density for model 4 (cf. Fig. 5). In this model a stable, constant density inner core is formed (solid lines), again hiding the profile found assuming fully disrupting collisions (dashed lines).

are in qualitative agreement with previous work; in particular, it was found that collisional mass production greatly exceeded that by tidal disruption when the former could support modest AGN activity. In fact, most tidal disruptions in these simulations were the result of collisional refilling of the loss cone, not refilling by relaxation effects.

One motivation for these simulations was to search for relativistic influences on cluster evolution around a massive black hole, which has previously been treated as a Newtonian point mass. Outside of the (small) mass loss rate due to stars on plunge orbits, however, little evidence for relativistic effects of any type was found in the results; in particular, the spin of the hole did not qualitatively alter any of the results, and no evidence of flattening due to the anisotropy of the Kerr metric (or anything else) was found. On balance, this is perhaps to be expected. One reason is that the presence of a tidal radius, which can lie well outside the horizon, prevents (intact) stars from closely approaching the hole, where relativistic effects are strong: although the tidal radius ranges anywhere from the horizon to $100M$ in these simulations (so that the maximum strength of relativistic effects varies between unity and $\sim 1\%$ between them), no correlations with this factor are found in the results. Also of probable importance is that colliding stars are randomly deflected (and eventually disrupted)—erasing any memory of effects such as relativistic precession, which are secular in nature and hence most noticeable when allowed to accumulate over long periods of time. This does not, however, detract from the promise of the general methods of simulation presented here, as their versatility allows them to be adapted to a range of problems. The statistical collision routine (§ 3.4) performed very well, and its ability to dynamically keep pace with a changing and possibly very anisotropic cluster distribution was only partially utilized. Also, nearly 'immortal' systems, such as clusters of compact objects dominated by relativistic relaxation instead of physical collisions, can in principle develop a long-term memory of previous interactions and allow the growth of secular effects to take place, and the deterministic collision algorithm (§ 3.3) does not require major modification to simulate this process.

An interesting issue outside the scope of this paper is the detailed physics of relativistic stellar collisions; e.g., qualitative changes in shock propagation and subsequent mass loss or unexpected modifications to collision-induced nuclear reactions might appear at extreme velocities. As the coexistence of dense nuclear clusters and massive black holes virtually guarantees that such collisions occur in nature, serious examination of this problem appears warranted.

Special thanks go to Melvyn Davies, who computed the SPH collision results used in the analysis, and to both him and Roger Blandford for discussions and suggestions on the manuscript. This work was supported by NSF grant AST92-23370, NSERC, and a Jeffrey L. Bishop Fellowship.

## A. Kepler's Equation in the Kerr Metric

This appendix derives a generalized form of Kepler's Equation valid for quasi-periodic geodesics in the Kerr metric to $O(\delta^{5/2})$, where $\delta = 1/[a(1-e^2)]$ (the inverse of the semi-latus rectum) is assumed to be a small parameter; also given is a compact, exact method for deriving a geodesic's constants of motion given its orbital elements. To our knowledge these results have not been published elsewhere. The results given in § A.3 can be considered a generalization of the work of Darwin (1961; see also Darwin 1959), who introduced the relativistic anomaly, $\chi$, which we will make use of, and essentially derived the modified form of Kepler's Equation valid to $O(\delta)$ in the Schwarzschild geometry, although he did not write the result in such a form or refer to it by that name.

### A.1. Equations of Motion in the Kerr Metric

The calculations explained below were done in a modified Boyer-Lindquist coordinate system with coordinates $(t, u, \mu, \phi)$ that are related to the standard Boyer-Lindquist coordinates $(t, r, \theta, \phi)$ by $u \equiv 1/r$ and $\mu \equiv \cos\theta$. As shown by Rauch & Blandford (1994), who also used these coordinates, the geodesic equations of motion in the modified coordinates take the form

$$p^t \equiv \frac{\mathrm{d}t}{\mathrm{d}\lambda'} = \rho^{-2}\left\{-j\left[j(1-\mu^2)-\ell\right] + \frac{(u^{-2}+j^2)}{\Delta}(u^{-2}+j^2-j\ell)\right\} \tag{A1}$$

$$p^\mu \equiv \frac{\mathrm{d}\mu}{\mathrm{d}\lambda'} = S_\mu \rho^{-2}\sqrt{M} \tag{A2}$$

$$p^u \equiv \frac{\mathrm{d}u}{\mathrm{d}\lambda'} = S_u \rho^{-2}\sqrt{U} \tag{A3}$$

$$p^\phi \equiv \frac{\mathrm{d}\phi}{\mathrm{d}\lambda'} = \rho^{-2}\left\{-j + \frac{\ell}{1-\mu^2} + \frac{j}{\Delta}(u^{-2}+j^2-j\ell)\right\}, \tag{A4}$$

where $U = (1-\gamma^{-2}) + 2\gamma^{-2}u + [j^2(1-\gamma^{-2}) - q^2 - \ell^2]u^2 + 2[(j-\ell)^2 + q^2]u^3 - j^2q^2u^4$, $M = q^2 - (\tilde{j}^2 + q^2 + \ell^2)\mu^2 + \tilde{j}^2\mu^4$, $\tilde{j}^2 = j^2(\gamma^{-2}-1)$, $\rho^2 = u^{-2} + j^2\mu^2$, $\Delta = u^{-2} - 2/u + j^2$, and $\{S_u, S_\mu\} = \pm 1$ are arbitrary signs. The (dimensionless) integrals of motion are $\ell \equiv L_z/E$, $q^2 \equiv Q/E^2$, and $\gamma^{-2} \equiv m^2/E^2$, where $L_z, E, m$, and $Q$—the angular momentum component, energy at infinity, rest mass, and Carter's constant, respectively—are the usual dimensional constants of motion. As before, the angular momentum of the hole itself is $j$, with $|j| \leq 1$. The normalization of the affine parameter $\lambda'$ is such that $p_t = -1$ and $p_\nu p^\nu = -\gamma^{-2}$ for all particles. All the formulae given in the following two sections were derived by suitable expansion and/or manipulation of the preceding equations of motion.

### A.2. Orbital Elements and Constants of Motion

Presented in this section is a simple, exact procedure for computing the constants of motion $\ell, q^2$, and $\gamma^{-2}$ for a generic quasi-periodic orbit, given the corresponding orbital elements $a, e$, and $i$; formal definitions of the orbital elements themselves are also given. First recall that quasi-periodic bound orbits occur when the quartic $U$, whose roots determine the radial turning points of the orbit, possesses four positive real roots (neglecting the special case $j^2q^2 = 0$) and the particle's radial motion is trapped between the two smallest roots (smallest in $u$ coordinates), say $u_{\rm max}$ and $u_{\rm min} < u_{\rm max}$; all such orbits have $\gamma^{-2} > 1$ and $q^2 \geq 0$. For these orbits the polynomial $M$ can be factored into $M = \tilde{j}^2(\mu_-^2 - \mu^2)(\mu_+^2 - \mu^2)$, where $0 < \mu_+ \leq 1 < \mu_-$; thus the $\mu$ coordinate is trapped between $\pm\mu_+$. We define the orbital elements $a$ and $e$ the same way they would be defined in the non-relativistic case, namely by setting $u_{\rm max} = 1/[a(1-e)]$ and $u_{\rm min} = 1/[a(1+e)]$. We see two reasonable ways in which to define the inclination of the orbit; if $j = 0$ the orbits are strictly planar and the definitions become equivalent (and agree with intuition), but for $j \neq 0$ they are slightly different. The two definitions are: $\tan i = \ell^{-1}\sqrt{q^2}$ and $\sin i = \mu_+$, with the additional condition that $i > \pi/2$ when $\ell < 0$. Numerically the two definitions agree to several digits even for highly relativistic orbits ($a(1-e) \sim 10$), so for our purposes it should not matter which one is used. In this paper the former expression was used as the definition of $i$ because of its simpler relation to the constants of motion.

Having formally defined the orbital elements, the method for computing the constants of motion from these elements—assuming the orbit they describe actually exists—can be derived in the following manner. Define the constant $b = (\ell^2 + q^2)^{1/2}$, which implies that $\ell = b\cos i$ and $q^2 = b^2\sin^2 i$. By writing $U$ in the form $U = -j^2q^2(u-u_1)(u-u_2)(u-u_{\rm max})(u-u_{\rm min})$ (where $u_{\rm max}(a,e)$ and $u_{\rm min}(a,e)$ are known), expanding, equating the resulting coefficients with the original expression for $U$ given in § A.1, and replacing $\ell$ and $q^2$ with their expressions in terms of $b$ and $i$, one obtains a system of equations from which $u_1, u_2$, and $\gamma^{-2}$ can be eliminated. One finally obtains a quadratic equation in $b$ with coefficients depending only on $a, e, i$, and $j$; after solving this equation for $b$, the values of $\ell, q^2$, and $\gamma^{-2}$ follow trivially. Note that the quadratic in $b$ would have been a *quartic* if not for a fortuitous cancellation. The equation determining $b$ is

$$B_2 b^2 - 2B_1 b + B_0 = 0, \tag{A5}$$

where

$$\begin{aligned}
B_0 &= 1 + j^2\delta^2[2(1+e^2) - 4\delta(1-e^2) + j^2\delta^2(1-e^2)^2], && \text{(A6)}\\
B_1 &= j\delta^2\cos i[(3+e^2) - 4\delta(1-e^2) + j^2\delta^2(1-e^2)^2], && \text{(A7)}\\
B_2 &= -\delta\Big\{[1-2\delta(1-e)][1-2\delta(1+e)] +
\end{aligned}$$

$$j^2\delta^2[-\delta(1-e^2)^2 + \sin^2 i\,\{2(1+e^2) - \delta(3-2e^2-e^4) + j^2\delta^2(1-e^2)^2\}]\Big\}, \tag{A8}$$

$\delta \equiv 1/[a(1-e^2)]$, and the positive root is to be taken. This procedure will always succeed even if the input orbit is invalid (e.g., if its traversal would require crossing the horizon), but in this latter case the values of $a$ and $e$ derived from the actual roots of $U$ will not be the same as those originally given the procedure, so a consistency check should be made for orbits passing close to the horizon ($\delta \gtrsim 0.1$, say). For $\delta \ll 1$ we have

$$\begin{aligned} b &= \delta^{-1/2}\{1 + 2\delta - j\cos i(3+e^2)\delta^{3/2} + [2(2+e^2) + j^2\cos^2 i(1+e^2)]\delta^2 \\ &\quad - 8j\cos i(1+e^2)\delta^{5/2} + O(\delta^3)\}. \end{aligned} \tag{A9}$$

The expressions for the constants of motion are $\ell = b\cos i$, $q^2 = b^2\sin^2 i$, and

$$\gamma^{-2} = \frac{1-\delta^3(1-e^2)^2[(1-j^2\delta)q^2 + (j-\ell)^2]}{1-\delta(1-e^2)}. \tag{A10}$$

For $\delta \ll 1$ we have

$$\gamma^{-2} = 1 + (1-e^2)\delta + (1-e^2)^2\delta^2 + (1-e^2)^2[1-e^2-(j-\ell)^2-q^2]\delta^3 + O(\delta^4). \tag{A11}$$

### A.3. The Modified Kepler's Equation

Following Darwin (1961), define a relativistic anomaly $\chi$ which is related to the particle's radial coordinate $u$ by

$$u(\chi) = \delta(1 + e\cos\chi), \tag{A12}$$

so that periapse and apoapse always occur at $\chi = 0$ and $\chi = \pi$, respectively, regardless of the amount of precession the orbit is undergoing. For nearly Newtonian orbits, $\delta \ll 1$, $\chi$ will be almost the same as the true anomaly $\nu$ familiar from celestial mechanics, and hence its time evolution will be closely approximated by Kepler's Equation,

$$\mathcal{M} = \psi - e\sin\psi, \tag{A13}$$

where the mean anomaly $\mathcal{M} = 2\pi t/t_{\rm orb} = t/a^{3/2}$ and the eccentric anomaly $\psi$ is related to the true anomaly by $(1+e\cos\nu)(1-e\cos\psi) = 1-e^2$. Clearly, by suitably expanding the equations of motion in powers of $\delta \ll 1$, the relativistic corrections to Kepler's Equation can be found; here they are given to $O(\delta^{5/2})$.

It is convenient to define a variable $\zeta$ according to

$$\zeta(\chi) = [j^2\mu_+^2(\gamma^{-2}-1)]^{1/2}\int_{u(\chi)}^{u_{\rm max}} \frac{{\rm d}u'}{\sqrt{U(u')}}, \tag{A14}$$

which upon expansion in $\delta$ becomes

$$\begin{aligned}\zeta(\chi) \;=\; & \{1 + 3\delta - 6j\cos i\,\delta^{3/2} + \tfrac{1}{4}\delta^2[54 + 3e^2 + j^2\cos^2 i\,(14 + e^2) - j^2(2 + e^2)] \\ & \quad - j\cos i\,\delta^{5/2}(42 + 3e^2)\}\chi + \\ & \{1 + \delta[9 + j^2(2\cos^2 i - 1) + e\cos\chi(3 - j^2\sin^2 i)/4] \\ & \quad - j\cos i\,\delta^{3/2}(34 + 3e\cos\chi)\}\delta e\sin\chi + O(\delta^3).\end{aligned} \tag{A15}$$

By inverting the integral relation $\int^{\mu} \mathrm{d}\mu'/\sqrt{M} = \int^{u} \mathrm{d}u'/\sqrt{U}$ to find $\mu$, one obtains the *exact* solution

$$\mu(\zeta) = \mu_+ \,\mathrm{sn}(\zeta_0 + \zeta \mid (\mu_+/\mu_-)^2), \tag{A16}$$

where $\mathrm{sn}(x \mid m)$ is a Jacobian elliptic function with parameter $m$ and the phase $\zeta_0$ is akin to the argument of periapse. Note that since

$$\mu_+ \;=\; \sin i\,[1 - j^2\cos^2 i\,(1 - e^2)\delta^2/2] + O(\delta^3), \tag{A17}$$

$$(\mu_+/\mu_-)^2 \;=\; j^2\sin^2 i\,(1 - e^2)\delta^2 + O(\delta^3), \tag{A18}$$

we have $\mu(\zeta) = \sin i\,\sin(\zeta_0 + \zeta) + O(\sin i\,\delta^2)$. Using this lower order expansion for $\mu$ when calculating the expansion for $\phi(\chi) = \int_0^{\chi}(\mathrm{d}\phi/\mathrm{d}u)(\mathrm{d}u/\mathrm{d}\chi)\,\mathrm{d}\chi'$ gives

$$\phi(\chi) = \phi_0 + \tan^{-1}(\cos i\,\tan\zeta) + \Delta\phi(\chi) + O(\sin i\,\delta^2), \tag{A19}$$

where $\phi_0$ is akin to the argument of the ascending node and

$$\begin{aligned}\Delta\phi(\chi) \;=\; & \Big\{[4 + (2 + e^2)(-j\cos i\,\delta^{1/2} + (6 + j^2)\delta)]\chi + \\ & [4 + (4 + e\cos\chi)(-j\cos i\,\delta^{1/2} + (6 + j^2)\delta)]e\sin\chi\Big\}\frac{j}{2}\,\delta^{3/2} + O(\delta^3).\end{aligned} \tag{A20}$$

In the mean plane of the orbit, which for a given periapse-to-periapse orbital segment was defined as the plane spanned by the position and velocity vectors at apoapse, the effective true anomaly is $\nu(\chi) \approx \zeta(\chi) + \cos i\,\Delta\phi(\chi)$, and thus the precession in the mean orbital plane per orbit is given by

$$\Delta\nu_{\mathrm{p}} = \nu(2\pi) - 2\pi = 2\pi(3\delta - 4j\cos i\,\delta^{3/2}) + O(\delta^2). \tag{A21}$$

The first term, $6\pi\delta = 6\pi/[a(1 - e^2)]$, is the well-known lowest order Schwarzschild value of the precession and the second represents the lowest order Kerr correction.

The concept of a (fixed) mean plane was found to be useful down to radii $r \sim 10$ (for $j \sim 1$), below which the perpendicular deviation of the true orbit from the mean plane over a single orbital period can be of order the radius itself. Since the errors in all of these formulae are secular in nature, to avoid accumulation of errors the collision finding algorithm (§ 3.3) used the accurate Kerr geodesic routines to reset $\zeta_0$ and $\phi_0$ to their optimum values for each orbital segment.

Finally, the modified form of Kepler's Equation follows from expansion and integration of $\mathrm{d}t/\mathrm{d}\psi = (\mathrm{d}t/\mathrm{d}u)(\mathrm{d}u/\mathrm{d}\chi)(\mathrm{d}\chi/\mathrm{d}\psi)$, where $\psi$ is now taken to be the eccentric anomaly corresponding to $\chi$, i.e., $(1 + e\cos\chi)(1 - e\cos\psi) = 1 - e^2$. Note that since the $\mu^2$ term in $\mathrm{d}t/\mathrm{d}u$ enters at $O(\delta^2)$, a solution accurate to $O(\delta^{5/2})$ need only use $\mu(\chi) \approx \sin i\,\sin(\zeta_0 + \chi)$ during the derivation. The result for $t(\chi)$ is

$$\begin{aligned}
\frac{t(\chi) - t_0}{a^{3/2}} \quad = \quad & \Big\{1 + 3(1 - e^2)\delta[1 - j\cos i\,\delta^{1/2}[1 + (7 - e^2)\delta] \\
& \quad + (2 + \tfrac{1}{2}j^2\cos^2 i)\delta]\Big\}\psi \\
& -\Big\{1 + (1 - e^2)\delta[-j\cos i\,\delta^{1/2}[1 + 2(2 - e\cos\chi)\delta] \\
& \quad + (2 + \tfrac{1}{2}j^2\cos^2 i)\delta]\Big\}e\sin\psi \\
& + \frac{1}{2}\Big\{[15 - 24j\cos i\,\delta^{1/2}]\chi - j^2\sin^2 i\,\cos(2\zeta_0 + \chi)\,\sin\chi\Big\}(1 - e^2)^{3/2}\delta^2.
\end{aligned} \tag{A22}$$

The value of the orbital period is simply $t_{\rm orb} = t(2\pi) - t_0$ which in addition to $a$ is seen to depend on both $e$ and $\zeta_0$. By rewriting the expansion using $\mathcal{M} = 2\pi t/t_{\rm orb}$, one arrives at the modified Kepler's Equation with errors $O(\delta^3)$,

$$\mathcal{M} = \psi - \tilde{e}\sin\psi + \Delta\psi, \tag{A23}$$

$$\begin{aligned}
\tilde{e} \quad &= \quad \Big\{1 - (1 - e^2)\delta\Big[3 - 2j\cos i\,\delta^{1/2}\{1 + (1 + 6e^2 + 6(1 - e^2)^{1/2} + e\cos\chi)\delta\} \\
& \qquad + \tfrac{1}{2}\delta(-10 + 18e^2 + 15(1 - e^2)^{1/2} + 2j^2\cos^2 i)\Big]\Big\}e,
\end{aligned} \tag{A24}$$

$$\Delta\psi \quad = \quad \frac{1}{2}\Big\{[15 - 24j\cos i\,\delta^{1/2}](\chi - \psi) - j^2\sin^2 i\,\cos(2\zeta_0 + \chi)\,\sin\chi\Big\}(1 - e^2)^{3/2}\delta^2. \tag{A25}$$

Because $0 \le \tilde{e} \le e$ and $\Delta\psi \sim O(\delta^2)$, the inverse solution $\psi(\mathcal{M})$ can be computed very economically by first finding the solution $\psi_0$ corresponding to $\Delta\psi \to 0$ and then correcting $\psi_0$ treating $\Delta\psi$ as a small perturbation, $\psi \approx \psi_0 - \Delta\psi_0/(1 - \tilde{e}\cos\psi_0)$. It was found that the relative error in the solution obtained in this way was normally no greater than that inherent in the expansion itself, except perhaps at larger distances, where the absolute error was still quite small. It was also found empirically that excluding the term involving $\zeta_0$ in $\Delta\psi$ and $\cos\chi$ in $\tilde{e}$ did not noticeably worsen the error in $\psi$ compared to its true value, allowing an additional gain in efficiency. This allowed the inverse solution $\psi(\mathcal{M})$ to be computed with little more work than is needed in the Newtonian case, greatly improving the performance of the collision finding procedure.

## B. Collision Products Fitting Formulae

The outcome of a collision between a pair of stars, characterized by the mass loss, angular deflection, and change in speed and radius suffered by each, was computed (except for the new radius, see below) from fitting formulae derived from the results of SPH simulations of high velocity stellar collisions performed for this work by Davies (1994). The fits to each of the derived quantities depended on three dimensionless variables describing the circumstances of the collision: the mass ratio, $q$, the relative velocity of the stars, $\beta_{\rm rel}$, and the impact parameter in units of the sum of the stellar radii, $\tilde{b} = b_{\rm min}/(R_{\star,1} + R_{\star,2})$ (where $b_{\rm min}$ is the minimum encounter distance), each of which ranges from 0 to 1. The relative speed as well as the vector changes in each star's velocity were computed in the orthonormal center-of-mass frame, each star's 4-velocity being transformed from the Boyer-Lindquist coordinate frame to the center-of-mass frame and back using the expressions appropriate for the Kerr metric at the point of collision.

Useful fitting functions could not be obtained for the change in radii because of noise limitations in the hydrodynamic results as well as physical uncertainties about the post-encounter equilibrium state of the star. Additionally, the post-encounter radius is likely to vary (shrink) with time as the star sheds any excess thermal energy acquired during the collision, which will occur on a Kelvin-Helmholtz timescale ($\sim 10^7$ years for solar type stars). Because of these inherent uncertainties, the new radius was crudely approximated as being equal to that of a main sequence star having the same mass as the surviving star. Although the actual surviving fragment will probably be somewhat larger than this initially, those outer layers will also be less dense and more loosely bound than an unperturbed main-sequence envelope, leading to less deflection and mass loss during glancing collisions. Hence it is reasonable to use the smaller radius in subsequent calculations, since any collisions resulting from the additional cross section presented by the outer layers will do little damage to the star in any case.

Most of the SPH simulations used $q = 1$ to determine basic dependence of the derived values on $\beta_{\rm rel}$ and $\tilde{b}$; estimation of the $q$ dependence of the results was based on a smaller number of simulations in which models originally using $q = 1$ were redone using $q = 1/2$ and $q = 1/4$. The stars were taken to be $n = 3$ polytropes. The fitting formulae are (it is assumed $q = m_2/m_1 < 1$)

$$\frac{\delta m_1/m_1}{\delta m_2/m_2} \approx q^{0.9}, \tag{B1}$$

$$\frac{\delta m}{m} = \frac{\delta m_1 + \delta m_2}{m_1 + m_2} \approx q^{0.2} \beta_{\rm rel}^{1.25} \exp[P_1(\tilde{b})], \tag{B2}$$

$$\delta\theta_1 \approx \delta\theta_2 \approx [\pi - 2/(P_2(\tilde{b}) + P_3(\tilde{b})\,\beta_{\rm rel}^{-2})] q^{-0.3}, \tag{B3}$$

$$\frac{\delta v_1}{v_1} \approx \frac{\delta v_2}{v_2} \approx \beta_{\rm rel}^{-2.75}\exp[P_4(\tilde{b})] + \beta_{\rm rel}^{-0.5}\exp[P_5(\tilde{b})], \tag{B4}$$

where $P_1(\tilde{b}) = 5.5530 - 2.8607\tilde{b} - 10.5255\tilde{b}^2$, $P_2(\tilde{b}) = 0.57366 + 0.18251\tilde{b} - 0.13155\tilde{b}^2$, $P_3(\tilde{b}) = 10^{-6}(3.057 - 4.825\tilde{b} + 2.616\tilde{b}^2)$, $P_4(\tilde{b}) = -16.138 - 7.26\tilde{b}$, and $P_5(\tilde{b}) = 0.417 - 15.96\tilde{b}$. (Note that whenever $\delta m_i > m_i$, complete disruption is implied; in this case the star was simply removed from the simulation and its mass, $m_i$, added to the collisional mass loss tally. Also, for very low encounter velocities, $\beta_{\rm rel} \lesssim \beta_{\rm esc} \sim 0.002$, stellar mergers occur and hence the fitting formulae would not apply, but this is not relevant for the present simulations.) These fits reproduce the SPH results to within errors $\sim 10\%$; the true accuracy of the formulae as applied in the simulations described in this paper is not so easily quantified, mainly because of the need to extrapolate the results to relativistic impact velocities ($\beta_{\rm rel} \sim 0.1 - 0.5$), the maximum velocity for which SPH results were obtained being $\beta_{\rm rel} \sim 0.05$. However, since it is clearly not possible to compute detailed encounter models for each of the thousands of collisions occurring over the course of the simulations, some standardized strategy is necessary, and the use of hydrodynamics simulations to provide a quantitative foundation for calculating the collision products allowed as much microphysics as practically feasible to be injected into this part of the simulations.

## REFERENCES


Artymowicz, P., Lin, D. N. C., & Wampler, E. J. 1993, ApJ, 409, 592

Bacon, R., Emsellem, E., Monnet, G., & Nieto, J. L. 1994, A&A, 281, 691

Bahcall, J. N., & Wolf, R. A. 1976, ApJ, 209, 214

Bardeen, J. M. 1970, Nature, 226, 64

Bardeen, J. M., & Petterson, J. A. 1975, ApJ, 195, L65

Benz, W., & Hills, J. G. 1987, ApJ, 323, 614

Blandford, R. D. 1987, in Hawking, S. W., Israel, W., eds, 300 Years of Gravitation (Cambridge: Cambridge Univ. Press), p. 277

Blandford, R. D., & Znajek, R. L. 1977, MNRAS, 179, 433

Cohn, H., & Kulsrud, R. M. 1978, ApJ, 226, 1087

Colgate, S. A. 1967, ApJ, 150, 163

Darwin, C. 1959, Proc. Roy. Soc. Lond. A, 249, 180

———. 1961, Proc. Roy. Soc. Lond. A, 263, 39

David, L. P., & Durisen, R. H. 1989, ApJ, 346, 618

David, L. P., Durisen, R. H., & Cohn, H. N. 1987a, ApJ, 313, 556

———. 1987b, ApJ, 316, 505

Davies, M. B. 1994, private communication

Davies, M. B., Benz, W., & Hills, J. G. 1991, ApJ, 381, 449

———. 1992, ApJ, 401, 246

Duncan, M. J., & Shapiro, S. L. 1983, ApJ, 268, 565

Eckart, A., & Genzel, R. 1997, MNRAS, 284, 576

Evans, C. R., & Kochanek, C. S. 1989, ApJ, 346, L13

Faber, S. M., Tremaine, S., Ajhar, E. A., et al. 1997, AJ, 114, 1771

Ferrarese, L., Ford, H. C., & Jaffe, W. 1996, ApJ, 470, 444

Frank, J., & Rees, M. J. 1976, MNRAS, 176, 633

Genzel, R., Hollenbach, D., & Townes, C. H. 1994, Rep. Prog. Phys., 57, 417

Haller, J. W., Rieke, M. J., Rieke, G. H., Tamblyn, P., Close, L., & Melia, F. 1996, ApJ, 456, 194

Harms, R. J., Ford, H. C., Tsvetanov, Z., et al. 1994, ApJ, 435, L35

Hills, J. G. 1975, Nature, 254, 295

Hoyle, F., Fowler, W. A., Burbidge, G. R., & Burbidge, E. M. 1964, ApJ, 139, 909

Karas, V., & Vokrouhlický, D., 1993, MNRAS, 265, 365

Kormendy, J., & Richstone, D. 1995, ARA&A, 33, 581

Kormendy, J., et al. 1996, ApJ, 459, L57

Kumar, S., & Pringle, J. E. 1985, MNRAS, 213, 435

Laguna, P., Miller, W. A., Zurek, W. H., & Davies, M. B. 1993, ApJ, 410, L83

Lai, D., Rasio, F. A., & Shapiro, S. L. 1993, ApJ, 412, 593

Lauer, T. R. 1989, in Merritt, D., ed, Dynamics of Dense Stellar Systems (Cambridge: Cambridge Univ. Press), p. 3

Lauer, T. R., Ajhar, E., A., Byun, Y.-I., et al. 1995, AJ, 110, 2622

Lee, H. M., & Nelson, L. A. 1988, ApJ, 334, 688

Lee, M. H. 1993, ApJ, 418, 147

Lightman, A. P., & Shapiro, S. L. 1977, ApJ, 211, 244

Lynden-Bell, D. 1969, Nature, 223, 690

Misner, C. W., Thorne, K. S., & Wheeler, J. A. 1973, Gravitation (San Francisco: W. H. Freeman Co.), Chapter 33

Murphy, B. W., Cohn, H. N., & Durisen, R. H. 1991, ApJ, 370, 60

Peebles, P. J. E. 1972, Gen. Rel. and Grav., 3, 63

Penrose, R. 1969, Rev. Nuovo. Cimento, 1, 252

Pringle, J. E. 1992, MNRAS, 258, 811

Quinlan, G. D., & Shapiro, S. L. 1989, ApJ, 343, 725

———. 1990, ApJ, 356, 483

Quinlan, G. D., Hernquist, L., & Sigurdsson, S. 1995, ApJ, 440, 554

Rauch, K. P. 1995, MNRAS, 275, 628

Rauch, K. P., & Blandford, R. D. 1994, ApJ, 421, 46

Rees, M. J. 1984, ARA&A, 22, 471

Richstone, D. O., Bower, G., & Dressler, A., 1990, ApJ, 353, 118

Sanders, R. H. 1970, ApJ, 162, 791

Spitzer, L., & Saslaw, W. C. 1966, ApJ, 143, 400

Spitzer, L., & Stone, M. E. 1967, ApJ, 147, 519

Syer, D., Clarke, C. J., & Rees, M. J. 1991, MNRAS, 250, 505

Thorne, K. S. 1974, ApJ, 191, 507

van der Marel, R. P., de Zeeuw, P. T., Rix, H.-W., & Quinlan, G. D. 1997, Nature, 385, 610

Young, P. J. 1980, ApJ, 242, 1232

This preprint was prepared with the AAS LaTeX macros v4.0.